Characterization of 3D printed PLA with the help of Mechanical, Di-electric and X-ray Diffraction techniques

by

Sai Sri Nidhi Munaganuru

Presented to the Faculty of the Graduate School of
The University of Texas at Arlington
in Partial Fulfillment of the Requirements
for the Degree of

MASTER OF SCIENCE IN AEROSPACE ENGINEERING

THE UNIVERSITY OF TEXAS AT ARLINGTON

May 2019

Supervising Committee:

Dr. Kenneth Reifsnider, Supervising Professor
Dr. Leila Ladani
Dr. Wen Shen

Acknowledgements

This thesis is based on research work conducted at the Institute of Predictive and Performance Methodologies department of The University of Texas at Arlington Research Institute.

I am truly grateful to Dr. Kenneth Reifsnider for being such an amazing mentor and for never ending enthusiasm towards research. This work would not have been possible without the generous support and guidance of Dr. Rassel Raihan, Muthu Ram Prabhu Elenchezhian, Vadlamudi Vamsee. I am grateful to my colleague Sabarinathan Pushparaj Subramaniyan who kept me motivated throughout my research.

I would also like to thank the members of my committee: Dr. Leila Ladani and Dr. Wen Shen for their time, support, and input as the project progressed. I would also like to acknowledge the immense help and knowledge provided by Ron LaPosa and David Manivanh from the University of Texas at Arlington Research Institute.

A special thanks to all the faculty in the Aerospace Engineering Department for creating an enjoyable working environment. I would like to thank to Institute of Predictive and Performance Methodologies at the University of Texas at Arlington Research (IPPM-UTARI) for its financial support. Finally, I would like to thank my parents, family and friends for their undying support and motivation.

Abstract

Characterization of 3D printed PLA with the help of Mechanical, Di-electric and X-ray Diffraction techniques

Sai Sri Nidhi Munaganuru, MS Aerospace Engineering

The University of Texas at Arlington, 2019

Supervising Professor: Dr. Kenneth Reifsnider

Additive manufacturing (AM) revolutionized many industries, i.e., Automotive, Biomedical, Aerospace and Defense. As opposed to traditional manufacturing methods, a part is manufactured layer by layer from 3D CAD models in AM. Though the vision of AM is impressive, there are many challenges that are hindering the widespread use of these complex parts. One of the main challenges is its strength that varies with different manufacturing parameters. We are going to investigate the effect of build parameters on the mechanical, electrical and crystalline properties of the additively manufactured heterogeneous material system. The goal of the thesis is to find a correlation between the Mechanical (MTS), Di-Electric and Crystalline (XRD) properties of the 3D printed PLA at varying engineering parameters and find a way to improve these properties by changing the manufacturing parameters.

Table of Contents

Table of figures

List of Tables

Introduction

Additive manufacturing technology first emerged in the 1980s and was used to print plastic objects with a technique known as Stereo lithography (SLA). In SLA an ultraviolet light beam is used to selectively cure a photosensitive polymer to build up a part layer by layer. Later other processes for printing plastic objects emerged such as Fused Deposition Modeling (FDM).

It is a pretty common phenomena for AM technologies to use a computerized 3D modeling software and a G-code generating software for 3D printing. Once a 3D sketch is produced and saved in a STL file format, a unique Geometric code generator software converts the drawing into code for the machine to lay down or add successive layers of liquid, powder, sheet material or other, in a layer-upon-layer fashion to fabricate a 3D object.

According to a recent article in the Amazing AM (LLC)'s website (AM Basics, 2018), the term **AM** encompasses many technologies including subsets like 3D Printing, Rapid Prototyping (RP), Direct Digital Manufacturing (DDM), layered manufacturing and additive fabrication. Early use of AM in the form of Rapid Prototyping focused on preproduction visualization models. More recently, AM is being used to fabricate end-use products in aircraft, dental restorations, medical implants, automobiles, and even fashion products. While the adding of layer-upon-layer approach is simple, there are many applications of AM technology [1].

(Gibson, Rosen, & Stucker, 2010) state that over the years, materials have been altered to suit more closely the operating parameters of the different processes and to provide better output parts. As a result, parts are now much more accurate, stronger, and longer lasting and it is even possible to process metals with some AM technologies [2].

Fused Deposition Modeling (FDM)

(Benwood, Anstey, Andrzejewski, & K.Mohanty) define FDM as a type of three- dimensional (3D) printing where a thermoplastic filament is heated above the melting temperature and then extruded onto a print surface in layers with the help of a heated nozzle. The nozzles trace the cross-section pattern for each particular layer with the thermoplastic material hardening prior to the application of the next layer. The process repeats until the build or model is completed and fascinating to watch [3]. A symbolic explanation of this process is shown in Figure-1. For additional support, specific materials may be required for some complex features. Similar to SLA,

the models can be machined or used as patterns. Fused Deposition Modelling has a lot of benefits like promoting sustainable, inexpensive development with decreased material waste, eliminating tooling requirements, and a significantly shorter supply chain. The rapid commercialization of such 3D printers has led to the increase in home usage creating a need to understand the properties of the materials being printed, specifically for structural purposes [4,5].

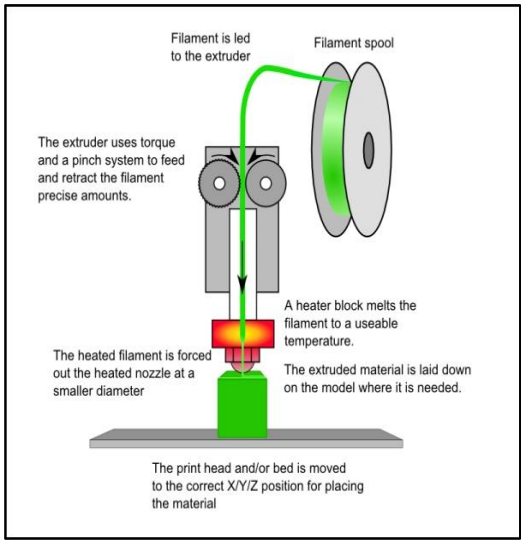

Figure 1: Process of fused Deposition Modeling

Certain things to keep in mind while selecting a material for FDM Process:

How well a part prints and the consequential properties of the printed parts is highly dependent on the material properties. The properties of concern include, Melting Temperature (Tm), Glass Transition Temperature (Tg), and the coefficient of thermal expansion (CTE). The melting temperature will play a major role in deciding the temperature that the extruder needs to be at to print the material. The amount of thermal stress developed during printing is related to the CTE and Tg. The strength and ductility of the printed part are also directly affected by the chemistry and microstructure [6].

Various Manufacturing/Build Parameters affecting material properties

Infill:

Infill is a support structure that is printed inside an object to increase its strength.

Infill % or Infill Density

Infill Density to set the density of your printed object's internal support structure. A higher percentage will result in a heavier, stronger object.

Shape of Infill

- **Hexagonal infill** is strong, so you can print sturdy objects without adding weight.
- **Linear infill** is made up of parallel straight lines, perpendicular to the lines on the previous layer. Linear infill is fast to print and makes your tool path simpler.
- **Diamond infill** is designed to be strong and to print quickly.

Bed temperature

Platform Temperature setting, which you can use to set the temperature of the heated build plate.

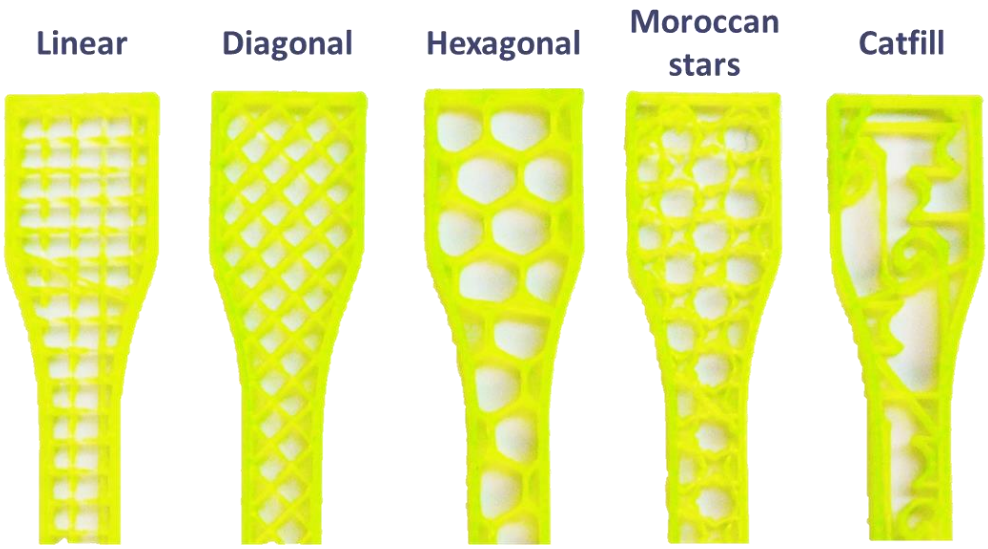

Figure 2: Different Infill shapes in 3D Printing

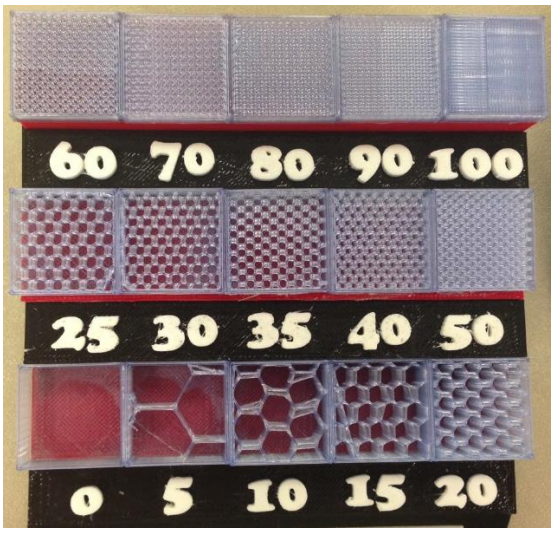

Figure 3: Effect on Infill Density/Percentage on 3D Printed samples

Material

The material we chose for the experimentation part of this thesis was Poly (Lactic Acid) (PLA). PLA is a rigid thermoplastic polymer that can be semi- crystalline or totally amorphous, depending on the stereo purity of the polymer backbone. PLA is the most commonly used polymer in 3D printing. It is preferred for its ease of printing, flexibility and its fairly low cost [7].

Since lactic acid is naturally produced and removed by the human body, some grades of PLA are used for medical implants that are intended to harmlessly break down over time and be replaced by growing tissue. The chemical monomer produced by most natural fermentation is the levorotory enantiomer and polymerizes to the bioactive Poly-L-lactic acid (PLLA) [6].

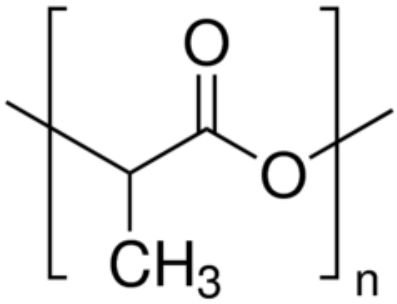

Figure 4: Chemical structure/monomer unit of PLA

Some Important information about PLA:

Table 1: PLA Material Specifications [6]

Chemical Formula	$(C_3H_4O_2)_n$
Crystallinity	37%-40%
Glass Transition	60-65^{0}C
Melting Temperature	150-160°C
Printing Temperature	178-240°C
Density	1.210-1.430g/g/cm3

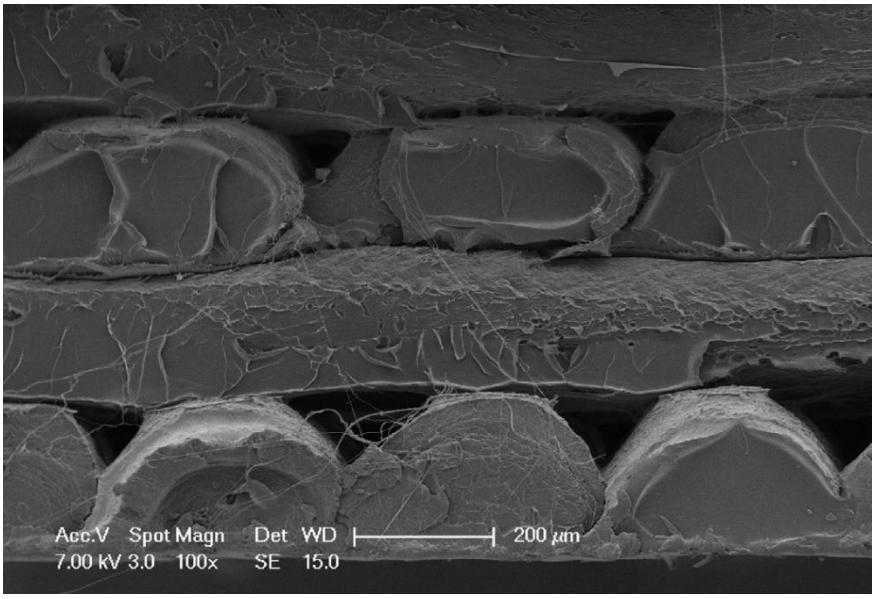

Figure 5: Scanning electron image of a white PLA sample 3D printed at 190 C showing the first four layers of the print with the bottom of the image corresponding to the bottom of the part when printing [8].

Motivation and background

In a recent article (Williams, 2018) quoted, "What was once used to manufacture small objects, figurines and vehicle prototypes is now being used to construct affordable and emergency housing in developing countries." In the same article another quote, "There are certainly discussions about 3D printing creating a low-cost alternative to housing construction, which can assist in the affordability crisis we're seeing. That said, I think it is not a short-term solution," Jerry Neuman said. "We haven't really been able to create the body of regulations that would be necessary to ensure its safety or have those processes evaluated" [9].

The first step to develop such safety evaluation procedures would be to look at the structures at an internal level.

Literature Review

Crystallinity:

(ROBSON, 2018) defined Crystallinity as a property of all polymers to be able to form organized 3D structures with polymer chains. A polymer's degree of crystallinity is the amount of the polymer that is ordered in a crystalline structure, given as a percentage. The remaining part of the polymer is amorphous. The crystallinity of the material generally ranges from 10% to 80% and it should also be noted that a perfectly crystalline plastic is all but non-existent. The properties that are important to consider during 3D printing such as the thermal (melting temperature) and physical properties are all determined by the molecular structure of the polymer. An important insight to polymers is that the individual units of a polymer are linked by very strong covalent bonds. On the other hand, the bonds between separate polymer chains are relatively weak Van der Waals bonds. Van der Waals forces are short-range interactions; so the tighter the polymers can pack together, the stronger these interactions will be. [10]

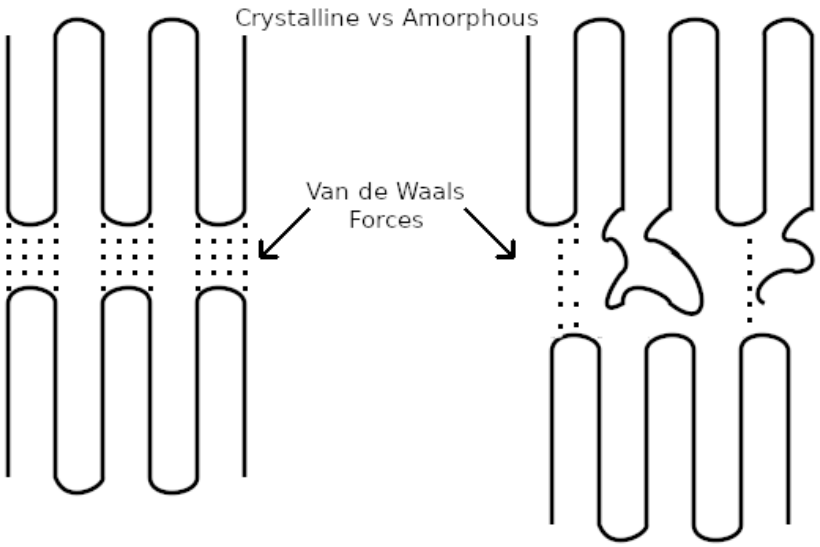

Figure 6: Comparison of Van De Waals forces for Crystalline vs Amorphous regions

(H.Tsuji & Y.Ikada, 1995) studied the effect of different thermal treatments and annealing histories on solution cast PLLA films, which resulted in materials with different morphologies and physical properties [11].

Crystallization:

The Polymers tend to exhibit high mobility when it reaches above the glass transition temperature. Over extended periods of time, they do not remain in the same position and they wiggle and squirm. They will give off enough energy to move into very ordered arrangements, which are called crystals. This formation of crystals happens when they reach the right temperature and give off heat. Hence there isn't a need to put out much heat to maintain the temperature of the sample pan rising. This drop is represented as a big peak in the heat flow in figure 7. The temperature corresponding to this peak point is the polymer's crystallization temperature, or Tc. Additionally the area of the peak defines the latent energy of crystallization of the polymer. The importance observation from this peak is that the polymer can crystallize. On the latter case, If an 100% amorphous polymer like polystyrene is analyzed, , this peak cannot be obtained, because they do not crystallize and also the polymer gives off heat when it crystallizes, called as crystallization is an exothermic transition.

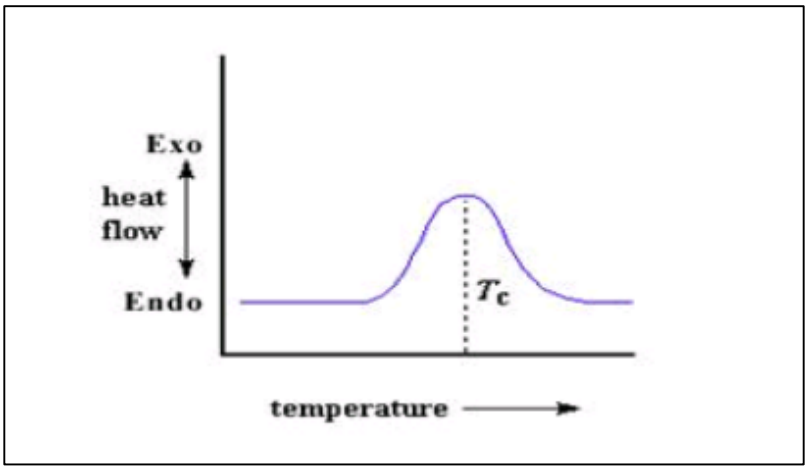

Figure 7: Representation of reaction occurring while Crystallization

Broadband Di-electric Spectroscopy and Permittivity Equations and Literature

To characterize these materials, mechanical and dielectric tests (using Broadband dielectric spectroscopy (BbDS) are performed on the printed parts. BbDS is a well- established tool for dielectric material characterization which has been used in polymer industries for a long time, e.g., in composite manufacturing this method is used to monitor the curing process. A material system is comprised of multiple polarization mechanisms such as ionic (molecular), dipolar

(orientational), electronic, interfacial (Maxwell–Wagner– Sillars) polarization and hopping charge polarization. The following Figure 8 shows the different types of polarization and their effect on the dielectric response and its corresponding effective frequency range. BbDS is the interaction of electromagnetic waves with matter in the frequency range from a lower value of 10^{-6} Hz to a higher frequency of 10^{12} Hz. This dynamic range contains information about the molecular and collective dipolar fluctuation; charge transport and polarization effects occur at inner and outer boundaries in the form of different dielectric properties of the material under study [12].

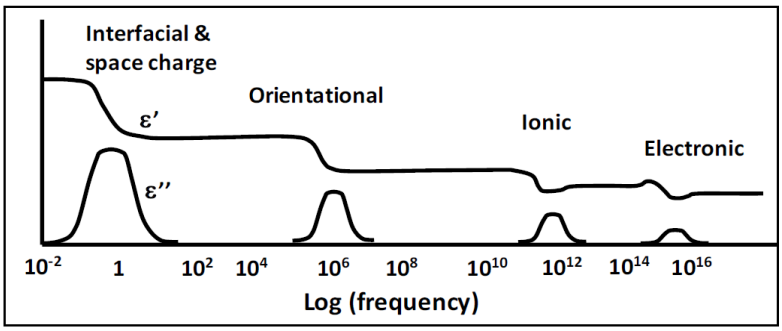

Figure 8 :- Effect of different charge displacement mechanisms on dielectric response and their corresponding effective frequency range

Polar molecules are contained inside of heterogeneous materials and in the presence of an applied electric field it will polarize the material by orienting the dipole moments of polar molecules and charge accumulation at the interfaces of dissimilar materials. The polarization of a linear dielectric is given as :

$$P = \varepsilon_0 \chi E \quad (1)$$

here, χ = tensor of dielectric susceptibility

ε_0 = dielectric permittivity of vacuum i.e., 8.854*10e-12 F/m

E = Electric Field.

Now, based on Maxwell's laws of electromagnetism, we have the equation,

$$\nabla \cdot D = \rho \quad (2)$$

This is also known as Gauss Law.

Displacement Field and ρ
The relation between the dielectric displacement and electric field is given as

From (1),

$$D = \varepsilon_0 E + P \text{ (3) } D = \varepsilon_0 E + \varepsilon_0 \chi E \quad (3)$$

$$D = \varepsilon_0 \varepsilon_r E \quad (3)$$

In this case, $\varepsilon_r = (1 + \chi)$ is known as relative permittivity. Finally, we get $D = \varepsilon E$ where $\varepsilon = \varepsilon_0 \varepsilon_r$ $_\Delta\varepsilon = \varepsilon' - \varepsilon''$ is defined as complex permittivity in which ε' is the real part of the complex permittivity and ε'' is the imaginary part, in other words the dielectric loss. Thus, we can now plot two graphs, one for the real part of the permittivity and other for the imaginary part, both of which corresponds to the logarithmic values of the frequencies.

The schematic of the setup is shown below in Figure 9. The arrangement is like a parallel plate capacitor, where in one end of the electrode an alternating signal is supplied, and the other end of the electrode is grounded.

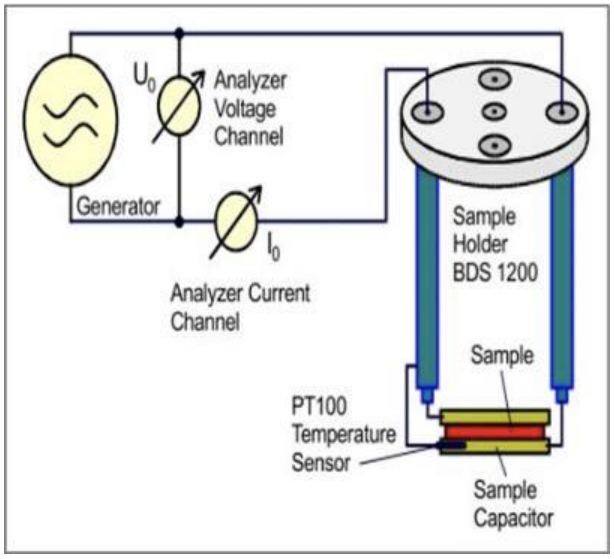

Figure 9: Effect of different charge displacement mechanisms on dielectric response and their corresponding effective frequency range. Schematic of the dielectric response setup

An AC voltage can be represented by equation 5.

$$U(t) = U_0 \cos(\omega t) = \mathrm{Re}(U^* \exp(i\omega t)) \quad (5)$$

Where $U^* = U_0$, is the amplitude of the signal applied, ω is the frequency of the applied signal. The measured current can be represented by equation 6.

$$I(t) = I_0 \cos(\omega t + \phi) = \mathrm{Re}(I^* \exp(i\omega t)) \quad (6)$$

$$I^* = I' + iI'' \quad (7)$$

$$I_0 = \sqrt{I'^2 + I''^2} \quad (8)$$

$$\tan(\varphi) = \frac{I''}{I'} \quad (9)$$

$$Z^* = Z' + iZ'' = \frac{U^*}{I^*} \quad (10)$$

Where I' is the real part of measured current, I'' is the imaginary part of measured current, φ is the measured phase lag, Z' is the measured real impedance of the material system, Z" is the imaginary part of impedance of the material system and the complex permittivity can be calculated by

$$\varepsilon^*(\omega) = \varepsilon' - i\varepsilon'' = \frac{-i}{\omega Z^*(\omega) C_0} \quad (11)$$

Where C_0 is the capacity of the empty sample capacitor.

Recently BbDS has been used by several researchers [13-15] to characterize composite materials and were able to study the relation of dielectric properties to material performance. (Raihan, Adkins, Baker, Rabbi, & and Reifsnider, 2015) used Dielectric Relaxation Strength (DRS) which is the algebraic difference between static permittivity value and the limiting frequency permittivity value as shown below in equation (12) to characterize the material.

$$\Delta\varepsilon = \varepsilon_s - \varepsilon_\infty \quad (12)$$

Higher DRS indicates more interfacial polarization owing to charge accumulation around boundaries (voids, cracks etc.), indicating a lower mechanical strength.

(Claudius Dichtl) worked on the Di-electric Properties of 3D printed Polylactic Acid. For the analysis of the material DSC and Dielectric Spectroscopy was performed. These properties were compared to precisely prepared samples of semi-crystalline and amorphous PLA. The dielectric properties of "as-printed" PLA were similar to the amorphous ones rather than the semi-crystalline

allowing good insulating properties below the glass transition temperature. Interestingly, DSC and dielectric measurements revealed that the mesoscopic structure of "as-printed" PLA, which is most likely influenced by the feeding mechanism of the 3D printer, also influences cold crystallization and maybe even the mobility or number of charge carriers. The latter showed a change in the onset temperature of a Maxwell-Wagner type relaxation process [16].

Introduction to X-Ray Diffraction

The electromagnetic radiation with typical photon energies in the range of 100 eV - 100 keV are defined as X-rays. Only short wavelength x-rays in the range of a few angstroms to 0.1 angstrom (1 keV - 120 keV) are used for the diffraction applications. They are typically suited for probing the structural arrangement of atoms and molecules in a wide range of structures as the wavelength of x-rays can be compared with the size of the atoms. They also provide valuable information about the bulk structure by penetrating deep into the materials and provide information about the bulk structure. [17]

X-rays are produced generally by either x-ray tubes or synchrotron radiation. X-rays are generated when a focused electron beam accelerated across a high voltage field bombards a stationary or rotating solid target in an x-ray tube. Bremsstrahlung radiation is a continuous spectrum of x-rays which are emitted when electrons collide with atoms in the target and slow down. Inner shell electrons in atoms are also ejected by the high energy electrons through the ionization process. When a free electron fills the shell, an x-ray photon with energy characteristic of the target material is emitted.

Diffracted waves from different atoms can interfere with each other and the resultant intensity distribution is strongly modulated by this interaction. The diffracted waves will consist of sharp peaks representing the interference maxima with the same symmetry as in the distribution of atoms, as the atoms are arranged in a periodic fashion. The distribution of atoms in a material is deduced by measuring the diffraction pattern.

The peaks in an x-ray diffraction pattern are directly related to the atomic distances. Figure 8 shows an incident x-ray beam interacting with the atoms arranged in a periodic manner in 2 dimensions

The atoms, represented as green spheres in figure 10 can be viewed as forming different sets of planes in the crystal. [17]

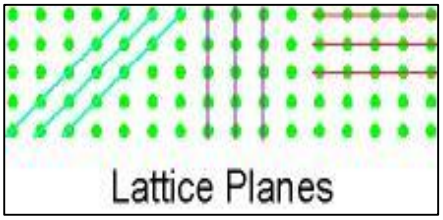

Figure 10: Representation of Lattice Planes

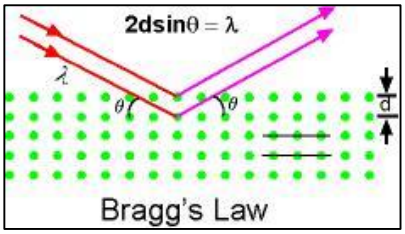

Figure 11: Representation of Bragg's law in a lattice plane

It is important to point out that although we have used atoms as scattering points in this example, Bragg's Law applies to scattering centers consisting of any periodic distribution of electron density. In other words, the law holds true if the atoms are replaced by molecules or collections of molecules, such as colloids, polymers, proteins and virus particles.

The response of a Crystal to a plane wave [18]:

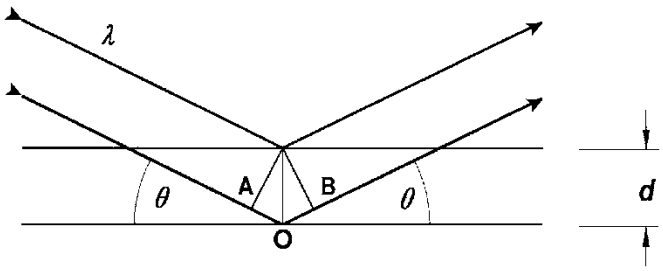

Figure 12: Diffraction of a plane wave off successive crystal planes

From figure 12 we can say that the Strong diffraction is a consequence when the angles of incidence and diffraction, are equal and the path difference AOB between the two beams is equal to n, an integral number of wavelengths. Any radiation striking a material is both scattered and absorbed. Scattering is most easily approached by thinking of a plane wave. This is formally defined as one whose phase is constant over any plane normal to its direction of travel, its wave front is a plane. It is more easily thought of as a point source of waves at an infinite distance; a perfectly collimated wave. When such a wave strikes a three- dimensional atomic lattice, each

scattering point (electron or nuclear particle) acts as a source of spherical waves, whose wave fronts lie on spheres centered on the scattering points. The addition of the amplitudes of all these waves in given directions results in almost zero intensity in most directions but strong beams in some directions if the wave-lengths of the wave are comparable with the spacing of the scattering centers. This is the phenomenon of diffraction.

The simplest and most useful description of crystal diffraction is still that obtained by Bragg. 2 Strong diffraction occurs when all the wavelets add up in phase. By considering an entire crystal plane as the scattering entity, rather than each individual electron, it is easy to see from figure (above) that strong diffraction results when

$$n = 2dsin\Theta \qquad (12)$$

where *n* is an integer representing the order of diffraction, is the wavelength, *d* the interplanar spacing of the reflecting (diffracting) plane and the angle of incidence and of diffraction of the radiation relative to the reflecting plane. The requirement for the angle of incidence to equal that of diffraction is not seen directly from Figure but arises from the incorporation of scattering from many planes normal to the surface. A small number of planes give a very broad peak, and large numbers of planes a narrow peak, converging to a value characteristic of a thick crystal. Thus, diffraction for a given plane and wavelength does not take place over the zero angular range defined by the Bragg law, but over a small finite range. This range, called the *rocking curve* width, varies tremendously and it governs the strain sensitivity of the technique.

High resolution X-ray diffractometry

The term 'Diffractometry' here means the measurement of the rocking curve of a sample. It is always necessary to define the incident radiation, both in wavelength and divergence, and a clear understanding of the latter is particularly important. The reference is always the plane wave rocking curve, such as would be measured with a perfectly parallel, monochromatic incident beam, and theoretical calculations are based upon this imagined radiation. Of course, any real radiation has both a wavelength spread and a divergence, and a good approximation to a plane wave curve is only found if the broadening effects of these are small compared with the width of the theoretical plane wave rocking curve. The rocking curve widths range from 0.6 to 12. The divergence of a

good synchrotron radiation beam could be about 1, and that of a sealed tube X-ray source at 1m is about 80. Synchrotron radiation is a continuous spectrum and single-crystal rocking curves map the spectrum. The rocking curve obtained in all other cases will be dominated by the source profile, little influenced by the specimen. In other words, the instrument function for conventional powder and single-crystal diffractometers is far too great to measure subtle changes in rocking curves of nearly perfect crystals.

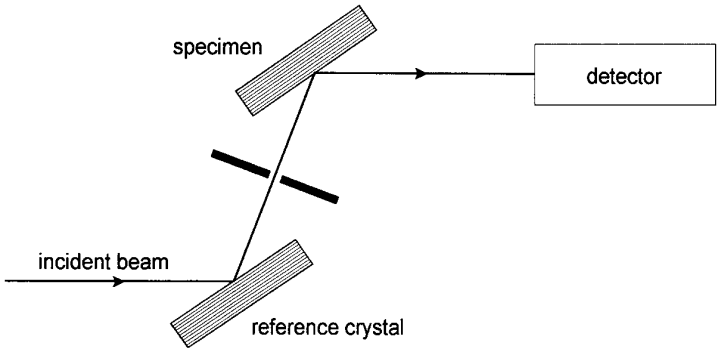

Figure 13: The symmetrical double crystal(+,-) setting for measuring rocking curves

From figure 13 the simplest conditioner is a perfect crystal of the same type as the specimen, using the same reflecting planes, with the deviation of the diffracted beam in the opposite sense to that at the specimen. This is the classic '+, − symmetrical double crystal method', as shown in Figure (above), which gives excellent and easily interpreted results.

Mechanical Testing for 3D printed specimens:

(O'Neal, 2015) worked on mechanical testing of 3D printed specimens with varying infill percentages. They found that the evolution of the specimen strength was not linear. With increase in infill percentage, the need for more material and more time arises which in turn affects the strength as well. According to their research, the ultimate surprise they had was that the elongation at break %, remained consistently at 2.8%, until 90% infill, where it dropped to 2.0. The explanation they provided for this phenomena was that with the much higher infill, 'faults' are created due to the lack of gaps in the mesh. Small 'air voids' cause strain, and thus, breakage, which seems specific to the 90% infill rate, yet with 'lower elongation at breakage.' At 100% there are no more voids and all of the filaments are touching. The yield stress test revealed the same results, thus validating the information on lower elongation breakage at 90% infill [19].

Experimental facilities

The thesis is divided into two stages. Stage -1 [20] represents the research work for a conference paper (ref) and Stage-2 refers to the advancement to research work of Stage-1.

Mechanical Testing Setup:

Axial Tension test was performed on the MTS© tensile testing machine equipped with 50 KN load cell and hydraulic wedge grips at IPPM UTARI. The gripping pressure was approximately 25-200 psi (based on infill percentage) as shown in tables [2, 3] . Static axial tensile loading was applied using displacement control at a constant rate of 0.025mm-s^{-1}. The testing setup and a set of samples used for testing are shown in figures 14-16.

Stage-1:

Table 2: MTS testing grip pressures based on Infill Percentages for Stage-1

Infill Percentage (%)	**Grip Pressure(psi)**
12.5%	25
33%	50
50%	100
100%	150

Stage-2:

Table 3: MTS testing grip pressures based on Infill Percentages for Stage-2

Infill Percentage (%)	Grip Pressure(psi)
25%	150
50%	150
75%	200
100%	200

Figure 14: MTS setup

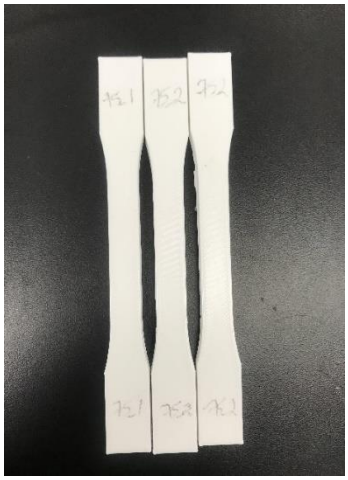

Figure 15: Stage-1 MTS Specimens

Figure 16: Stage-2 MTS specimens

Dielectric Testing Setup

Stage-1:

An in-house manufactured faraday cage was used to block out external interferences. The broadband dielectric/impedance spectrometer, manufactured by Novocontrol©, was used for carrying out the dielectric study. The sample was placed between two copper electrodes of 0.5-inch diameter embedded in blocks made of polycarbonate material. A voltage of 1.0 V is applied to the sample resulting in a flow of current with a phase shift. The dielectric properties of the material system are calculated using equations (9-11). Figure 17 shows the equipment setup that was used to carry out the experiments.

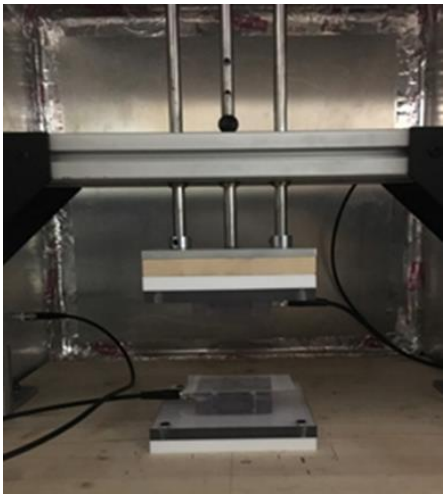

Figure 17: Stage-1 Faraday cage setup

Stage 2:

The Broadband Dielectric/Impedance Spectrometer, manufactured by Novo control, was used for carrying out the dielectric study. The sample was placed between two copper electrodes of 30mm and 40mm diameter. A voltage of 1.0 V is applied to the sample resulting in a flow of current with a phase shift. The dielectric properties of the material system are calculated using equations (9-11). Figure 18 shows the equipment setup that was used to carry out the experiments.

Figure 18: Stage-2 Novo Control Sample cell setup

3D Printer Setup

Stage 1:

The samples were printed using Lulzbot Taz at UTARI. The printer functions with Fused Deposition modeling along with an automatic Bed Levelling System. Some of its specifications are shown below in table 4. Figure 19 shows the printer setup and samples which are being printed.

Table 4: Lulzbot Taz 6 Specifications

Maximum Bed Temperature	120°C (248°F)
Print Bed area	280 mm x 280 mm x 250 mm (11.02 in x 11.02 in x 9.8 in)
Maximum Print Speed	200 mm/sec (7.9 in/sec)
Average Print Speed	30 - 50 mm/sec (1.18 - 1.97in/sec)
Printable Materials	PLA, ABS, PVA, HIPS, Polyester (Tritan), PETT, bronze

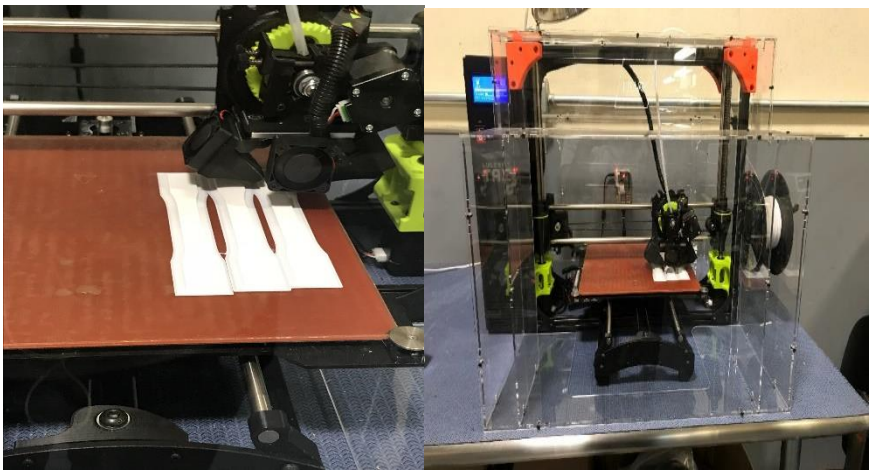

(a) (b)

Figure 19:- Specimen Preparation using Lulzbot Taz printer at UTARI

Stage 2:

Makerbot Replicator Z18:

A commercial 3D printer following the principles of Fused Deposition Modelling at the University of Texas at Arlington Research Institute was used to print the samples. Some of its important specifications are shown below:

Table 5: MakerBot Replicator Z18 Specifications

Print Technology	Fused Deposition Modeling
Build Volume	30.0 L x 30.5 W x 45.7 H CM [11.8 L x 12.0 W x 18.0 H IN]
Material Diameter	1.75 mm [0.069 IN]
Extruder Type	Smart Extruder+
Nozzle Diameter	0.4 MM [0.015 IN]
Print File Type	.MAKERBOT

Figure 20: MakerBot Replicator Z18

XRD equipment:

Siemens XRD D500

The Siemens D500 has earned a reputation for itself as one of the most reliable powder XRD systems ever designed and our refurbished units continue to be one of our bestselling models. These instruments are in use at many of the nation's largest national laboratories, industrial giants and academic institutions where they are relied upon daily for quantitative and qualitative analysis of everything from geological specimens to high explosives. Optional software upgrades unlock the full potential of XRD analysis with WPF (Rietveld), Semi-automatic phase analysis (Search/Match) and others. It uses **Data Scan4** software for testing.

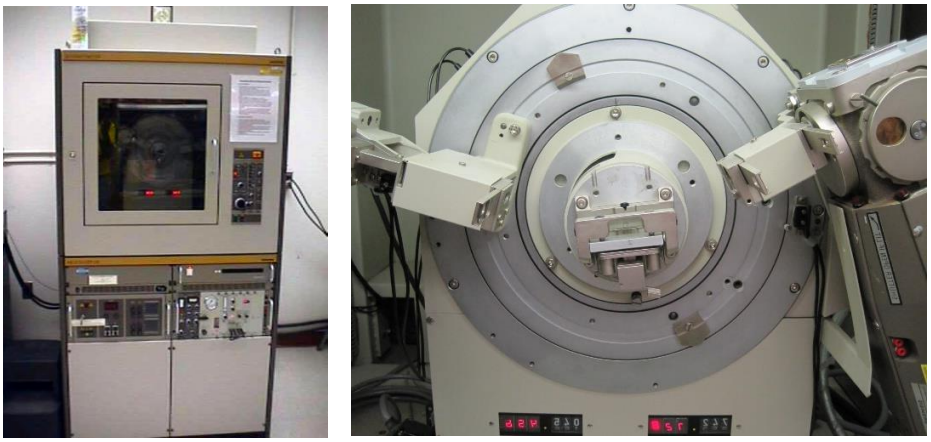

Figure 21: Siemens XRD D500

Peak fitting Software:

Origin Pro product from Origin labs has a unique Peak analyzer which helped to calculate % crystallinity for this thesis.

A few basic steps for Peak fitting using origin pro:

1. Smoothing: Using **Adjacent Averaging**, the XRD data can be smoothened which can help to define the crystalline peaks in a better way amongst the amorphous peaks.
2. Baseline: A baseline is chosen based on the start and end points of the XRD data, for the calculation of peak areas.

3. Peak Fitting: Using **Local Maximum method**, that compares the nearest N neighbors to find the maximum, we can find the crystalline peaks with the help of the software.
4. Area Selection: The next step is to select the area for each peak.
5. Integral Areas: The final step is to let the software calculate the integral of the areas under the crystalline peaks and also under the whole region.
6. Crystallinity % calculation: At the end we calculate the crystallinity % using the following formula

$$\textbf{Crystallinity \%} = \frac{\textbf{Integral of the area of the crystalline peaks}}{\textbf{Integral of the area of the total region}} \quad (14)$$

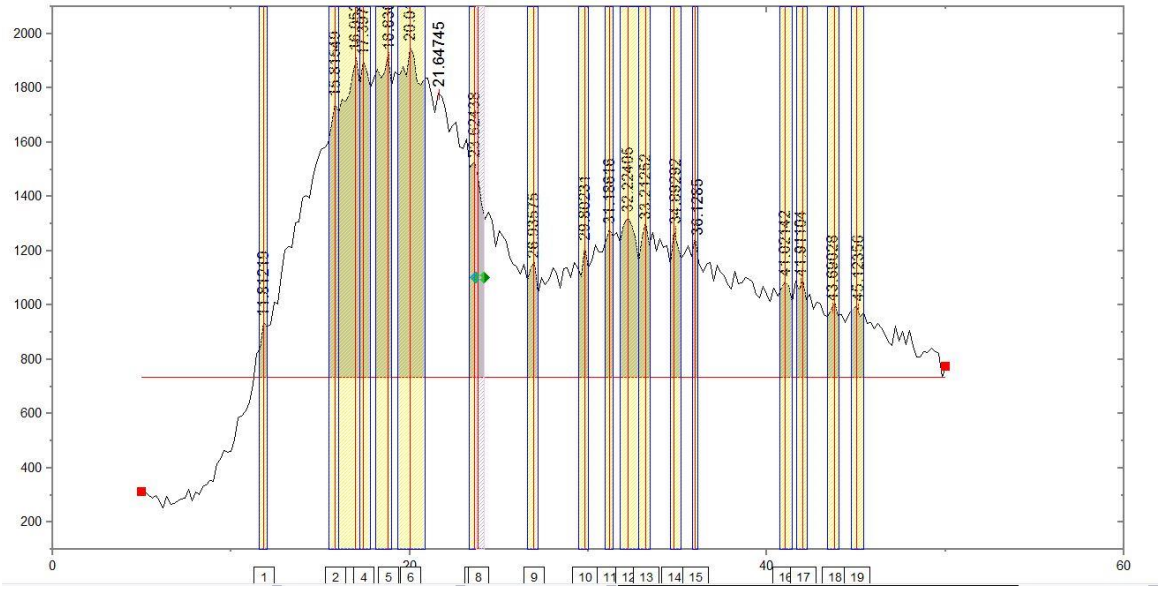

Figure 22: Representation of crystalline areas after peak fitting

Experimental procedure

Design of Experiments

Stage 1:

For the conference paper, the infill percentage and bed temperature were used as variables to determine their influence on the performance of the PLA material systems. Table 6 shows the tabulated values of various infill percentages and bed temperatures used for the study. For each case, 3 specimens were used to take in to consideration the statistics of each case.

Table 6: Design of experiments for Stage-1 with various infill percentages and Bed temperatures

Run Order	Infill %	Bed Temperature
1	12.5	50
2	12.5	75
3	12.5	80
4	33	50
5	33	75
6	33	80
7	50	50
8	50	75
9	50	80
10	100	50
11	100	75

Stage 2

For the next stage of this thesis, a fresh design of experiments was made using the student version of MINITAB software to maintain statistical standards. A total of 12 sets were generated using Factorial analysis from the software as shown below.

Table 7: Design of experiments for Stage-2 with various Infill percentages and Infill Shapes

Run Order	Infill%	Pattern
1	75	linear
2	25	linear
3	25	diamond
4	50	hexagonal
5	50	linear
6	100	linear
7	75	diamond

8	75	hexagonal
9	25	hexagonal
10	100	diamond
11	50	diamond
12	100	hexagonal

For each run-order/set 3 Mechanical test samples, 1 Di-electric sample and 1 crystallinity test sample was printed as seen below in figure 23.

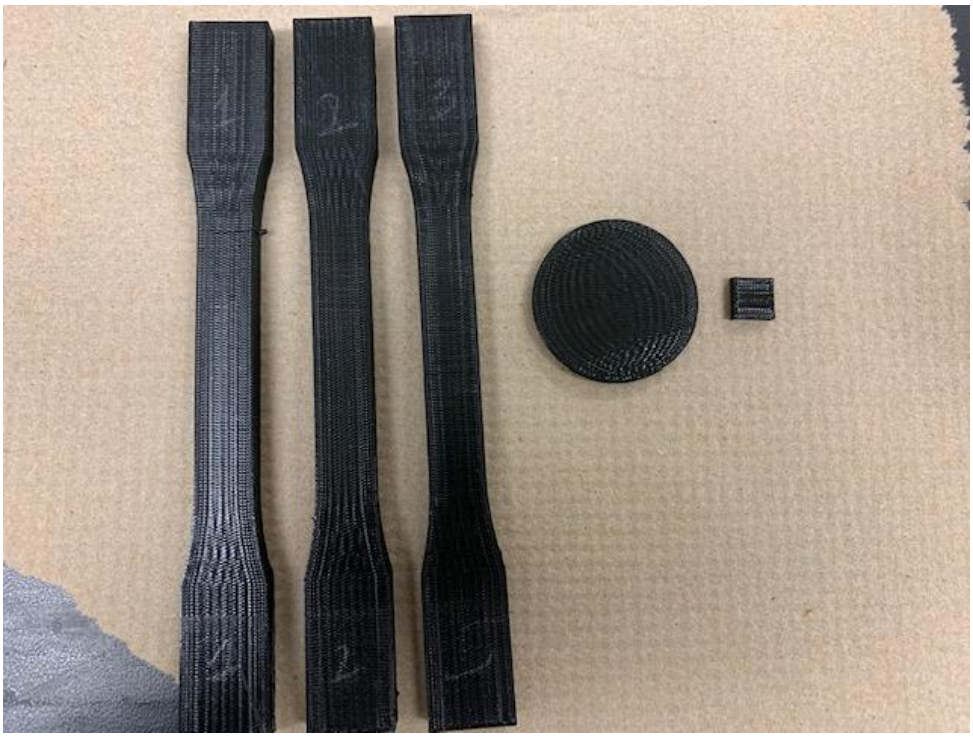

Figure 23: All the samples 3D printed for a particular set in Stage-2

3D Design

For both the stages of the thesis, a 3D model was designed using SolidWorks software at the University of Texas at Arlington Research Institute.

Specimen Preparation

The Mechanical and Di-electric sample were prepared the same way as described further.

Mechanical:

For practical applications, these 3D-printed parts must tolerate significant amounts of mechanical, thermal, environmental etc. loads and hence it is of great importance to determine the required strengths, and at the very least, the physical properties of these 3D-printed parts should be

comparable to those manufactured by conventional methods. Due to the nature of the process that builds the parts layer by layer, the mechanical properties of the part depend on the material used and processing parameters which include the raster orientation, extrusion temperature, bed temperature, infill percentage, patterns and many more. For mechanical testing the samples were designed following the ASTM D638 [21] Type-1 standards as shown in figure 24 with 7mm thickness.

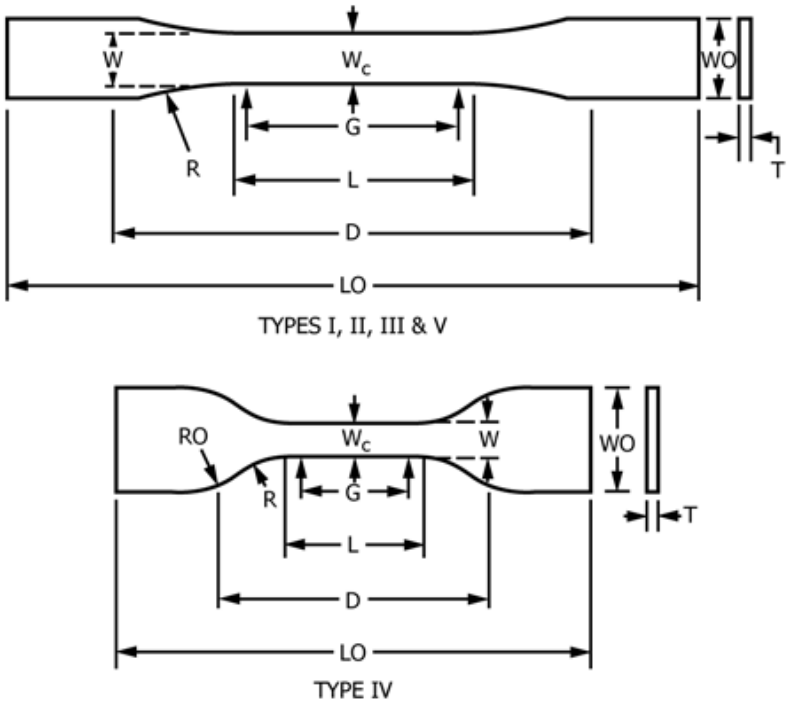

Figure 24: ASTM D638 MTS specimen Dimensions

Di-electric:

For the Di-electric testing circular samples of 40mm width with a thickness of 7mm were printed and the two surfaces were marked 25x25mm square on either sides and Two-Part Silver Epoxy (working time 10 minutes and curing time 48 hours) was spread in these squares as shown in figure 3 (b), to get good contact on the surfaces while performing the Dielectric tests.

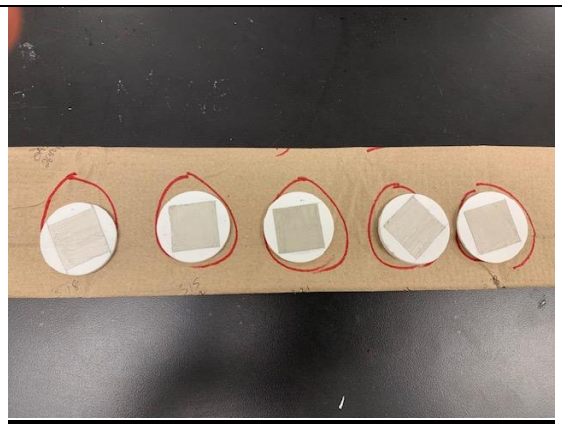

Figure 25: Stage-1 specimens prepared for Di-electric Testing

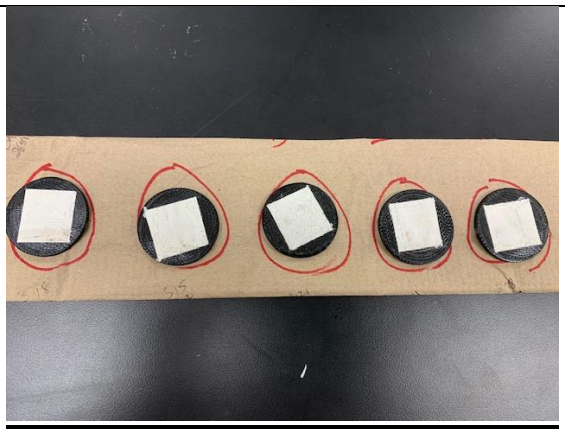

Figure 26: Stage-2 specimens prepared for Di-electric Testing

XRD testing

The 3D printed samples for this testing were 1x1 inch squares in dimension. This test was conducted only for Stage-2.

Scan Settings:

(WITTBRODT & PEARCE) have already done some work on XRD testing of 3D printed PLA [8].

- Following them, the scanning settings were: 5–50◦ (2θ) with count times of 2.5s per 0.2◦ (2θ
- Cu K$\propto$ radiation was used with scan settings
- [22] Standard procedures were followed during this testing.

Results & Discussion

Stage 1:

Results

A series of tensile tests were conducted on a set of AM fabricated samples with varying process parameters. Figure 277 shows the fractured set of specimens.

Figure 27:- Fractured set of specimens after mechanical testing for Stage-1

The observed mechanical and dielectric properties are tabulated below in table 8. The ultimate tensile strength (UTS) and DRS values of the experimental test data for each set is shown below. The axial displacement and axial force from the MTS test for various infill percentages at 50 °C bed temperature are shown in figure 28.

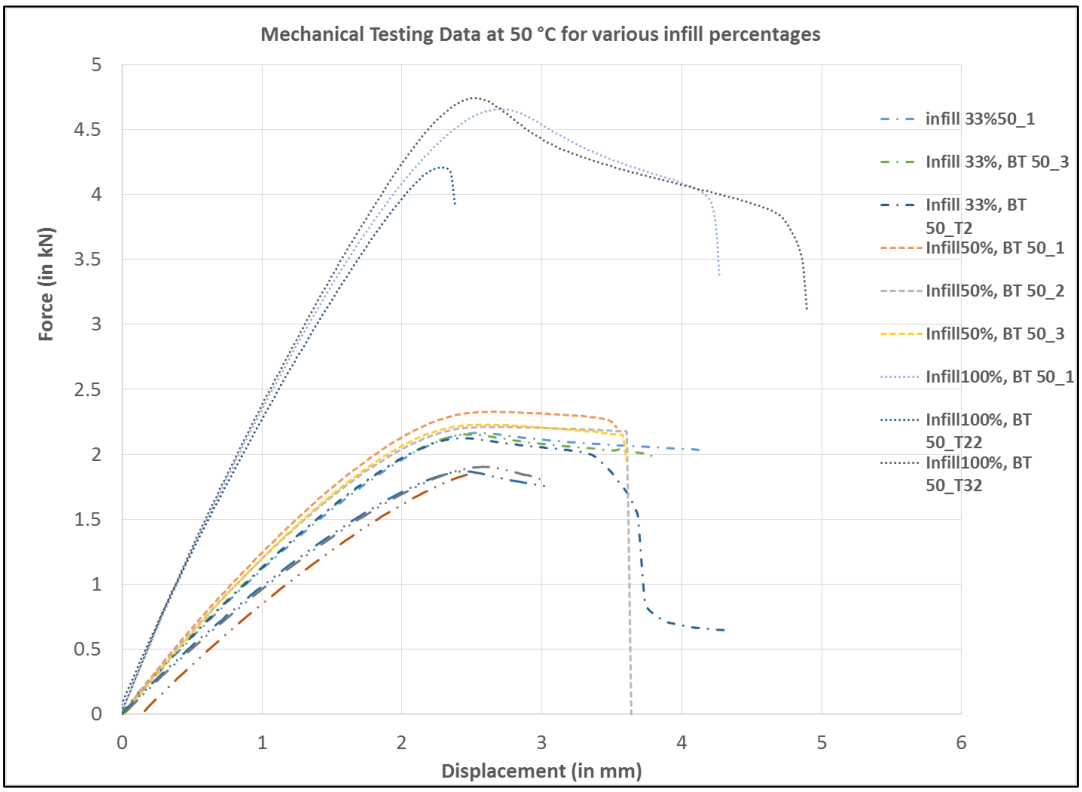

Figure 28: Force-Displacement plots at 50 °C for various infill percentages

Table 8: Tabulated results of Mechanical and dielectric testing for Stage-1

	Infill %	Bed Temp (°C)	UTS (MPa)	DRS
1	12.5	50	20.62	0.04
2		75	20.63	0.102
3		80	20.034	0.038
4	33	50	23.627	0.05
5		75	23.136	0.02
6		80	22.8	0.03
7	50	50	26.203	0.05
8		75	26.02	0.03
9		80	24.78	0.033
10	100	50	49.833	0.16
11		75	48.62	0.03

Discussion

From table 8, for 12.5 % infill set 2 (75°C bed temperature) specimens exhibited highest DRS values and had highest strength. This may be a result of material inflow across the voids due to high bed temperature. This additional material tends to reduce the internal residual stresses which ultimately increases the strength of the specimen. The permittivity as a function of frequency for various infill's at different bed temperatures are shown in 9.

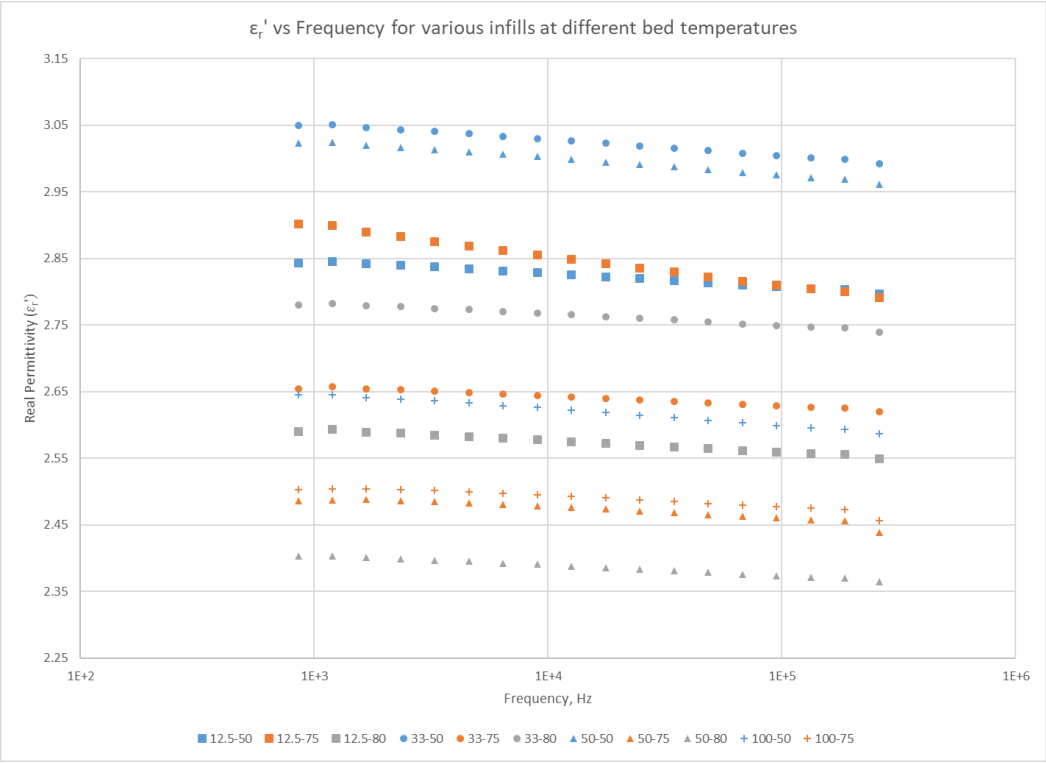

Figure 29:- Variation of real permittivity with frequency for various infill's at different bed temperatures

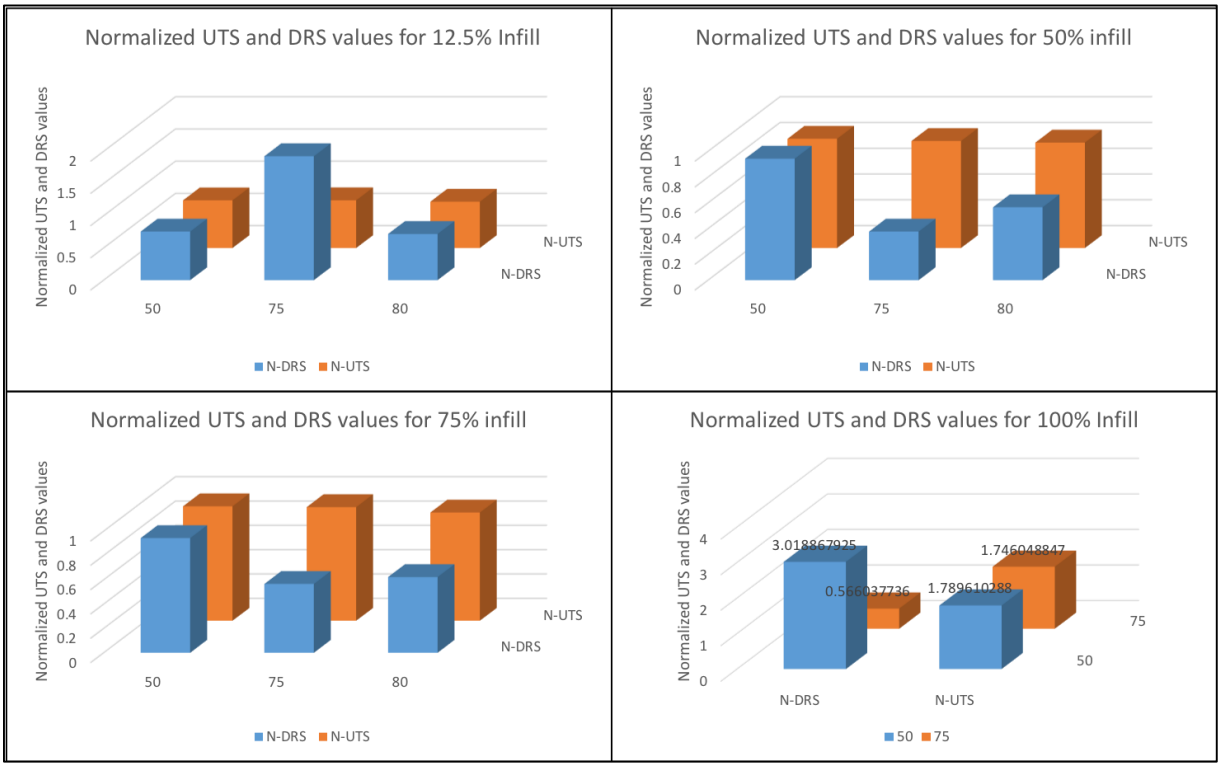

Figure 30: Comparison of mechanical and dielectric characterization for various infill's at different bed temperatures

From Fig 30, it can be observed that higher the DRS value, higher the ultimate tensile strength (UTS) in most of the cases with some discrepancies for 33 % and 50 % infill. This contradicts the observations made for polymer matrix composites by (Raihan et. al.,) which had different phases with different conductivity and permittivity where as these 3D printed coupons have only PLA filaments. This needs further analysis and will be published in subsequent journal publication

Stage-2

Results

A series of tensile tests were conducted on a set of AM fabricated samples with varying process parameters. Figure 31 shows the fractured set of specimens.

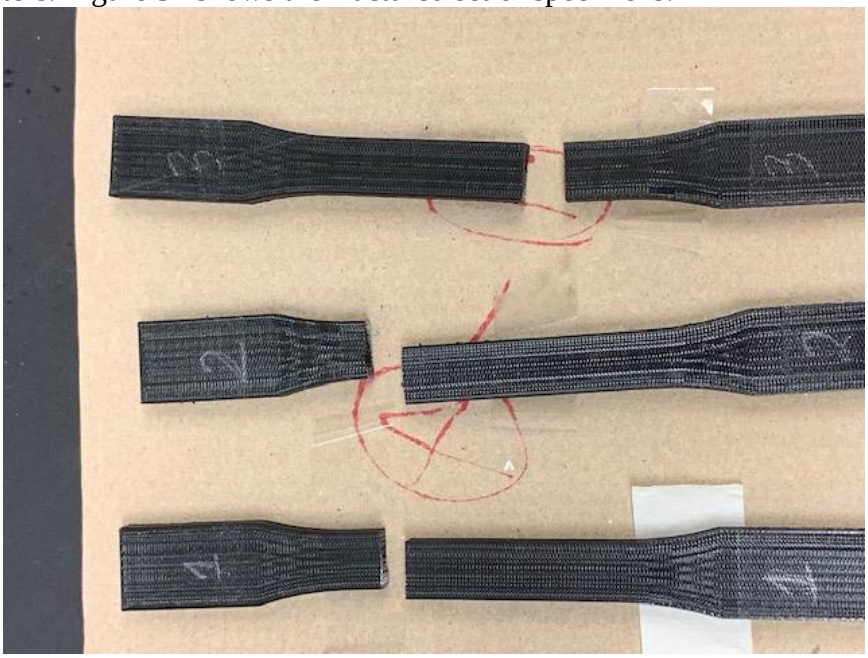

Figure 31: Fractured specimen of Stage-2

The observed mechanical and dielectric properties are tabulated below in Table 8.

Table 9: Average DRS and UTS values for Stage-2

Set	**Avg UTS**	**Avg DRS**
25%-linear	17.02552	7.12E-02
50%-linear	21.93299	1.12E-01
75%-linear	29.52417	1.50E-01
100%-linear	45.24648	1.93E-01
25%-diamond	16.54561	8.52E-02
50%-diamond	20.20971	1.29E-01
75%-diamond	26.54912	1.69E-01
100%-diamond	42.21658	1.71E-01
25%-hex	15.50941	8.52E-02
50%-hex	17.04071	9.87E-02
75%-hex	18.12687	1.05E-01
100%-hex	26.84906	0.180473333

The Stress vs. Strain% from the MTS test data for 3 sample of each infill % for Linear shape infill with varying infill percentages is shown in figure 32. The average Ultimate Tensile Strength values for Linear shape infill with varying infill percentages is shown in figure 33.

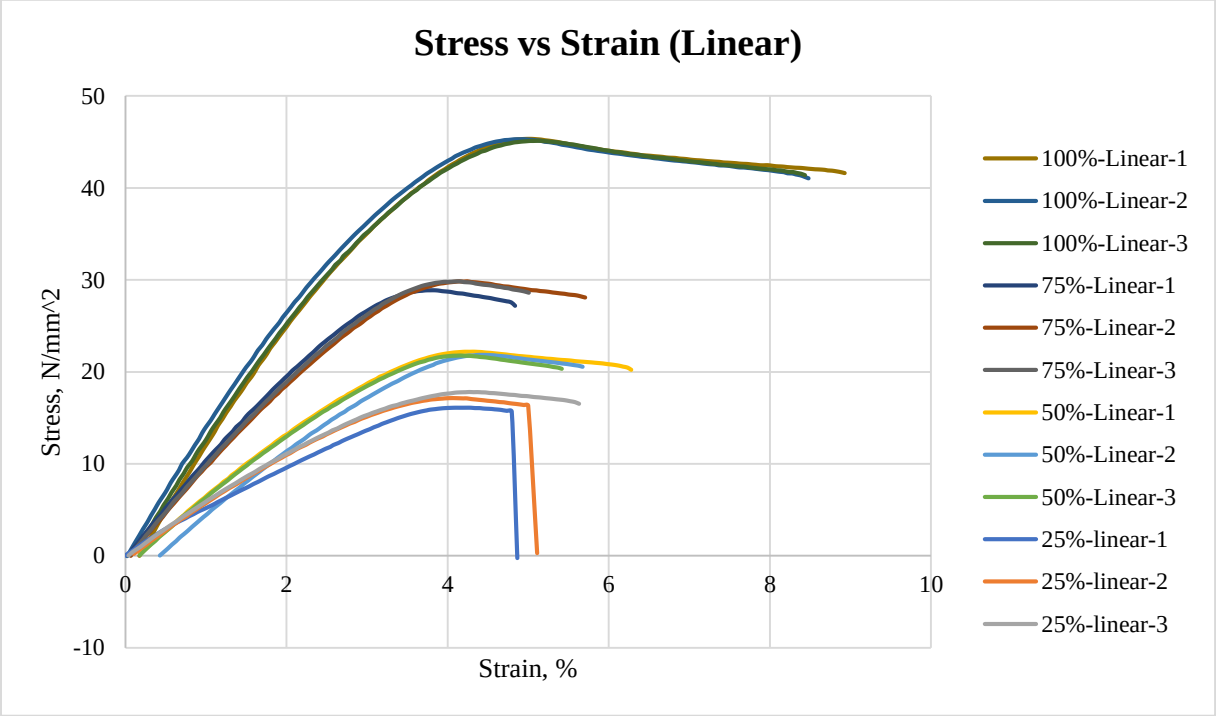

Figure 32: Stress vs. Strain for Linear shape infill with varying infill percentages

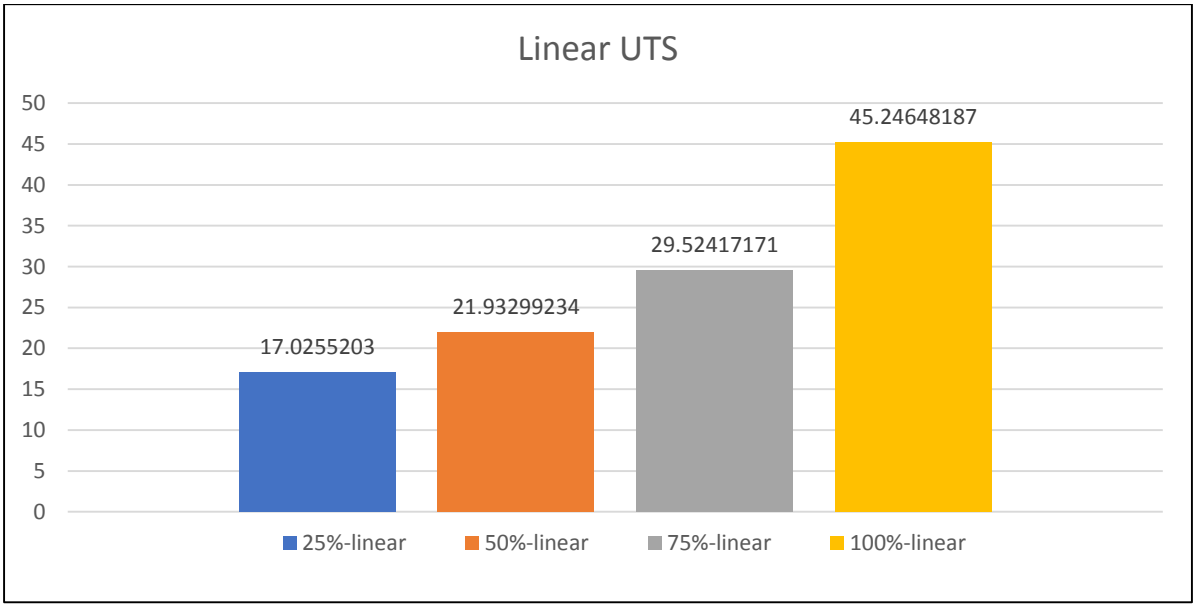

Figure 33: 2D histogram for UTS values of Linear shape infill

The Stress vs. Strain% from the MTS test data for Diamond shape infill with varying infill percentages is shown in figure 34. The average Ultimate Tensile Strength values for Diamond shape infill with varying infill percentages is shown in figure 35.

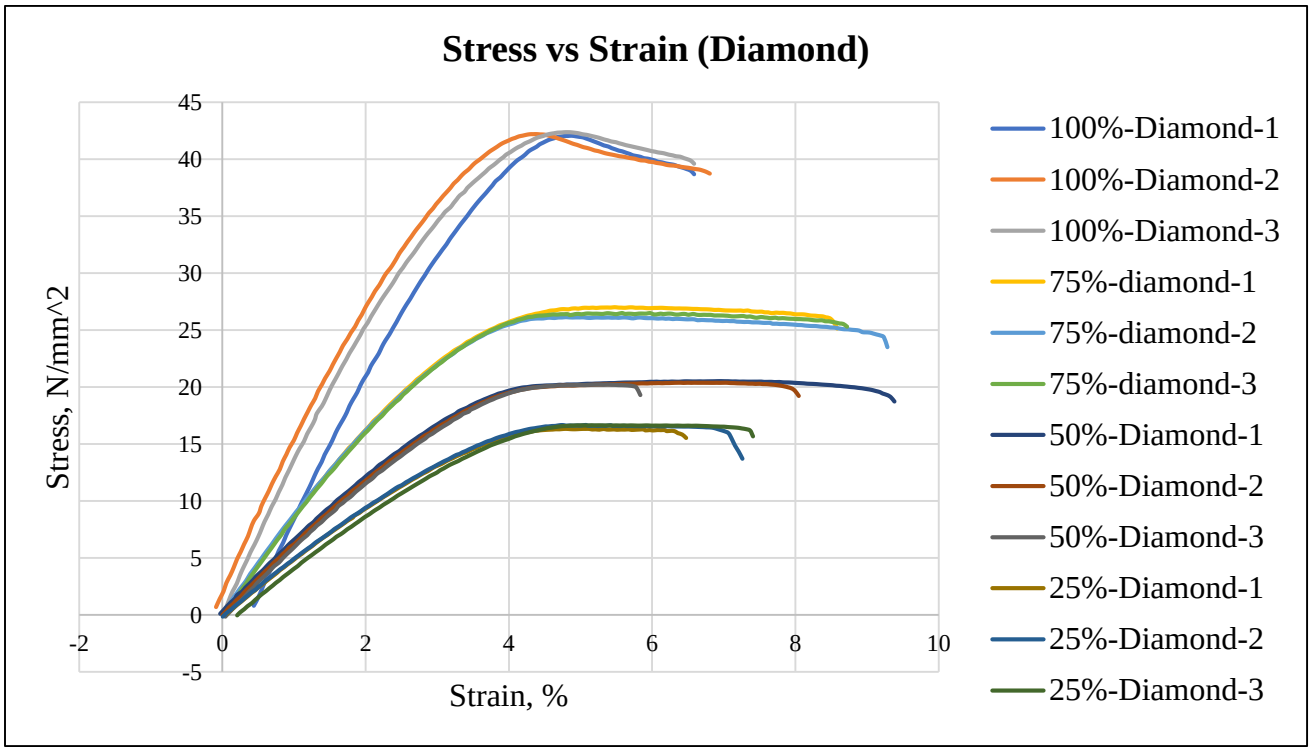

Figure 34: Stress vs. Strain for Diamond shape infill with varying infill percentages

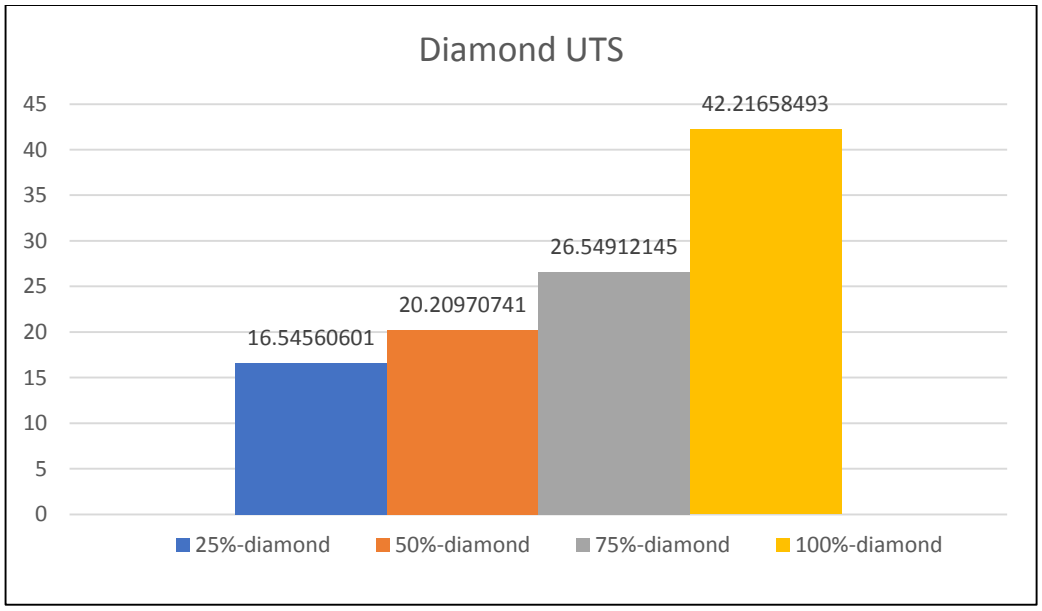

Figure 35: 2D histogram for UTS values of Linear shape Infill

The Stress vs. Strain% from the MTS test data for Hexagonal shape infill with varying infill percentages is shown in figure 36. The average Ultimate Tensile Strength values for Hexagonal shape infill with varying infill percentages is shown in figure 37.

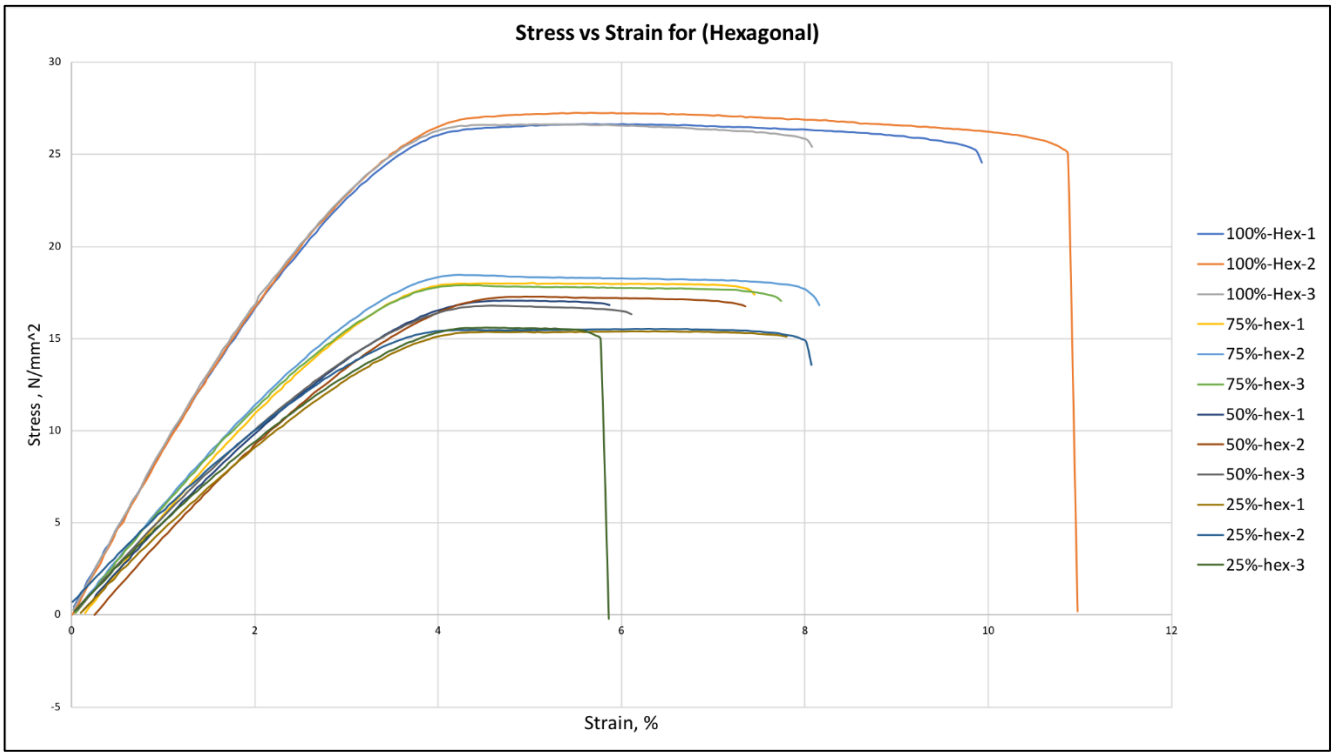

Figure 36: Stress vs. Strain for Hexagonal shape infill with varying infill percentages

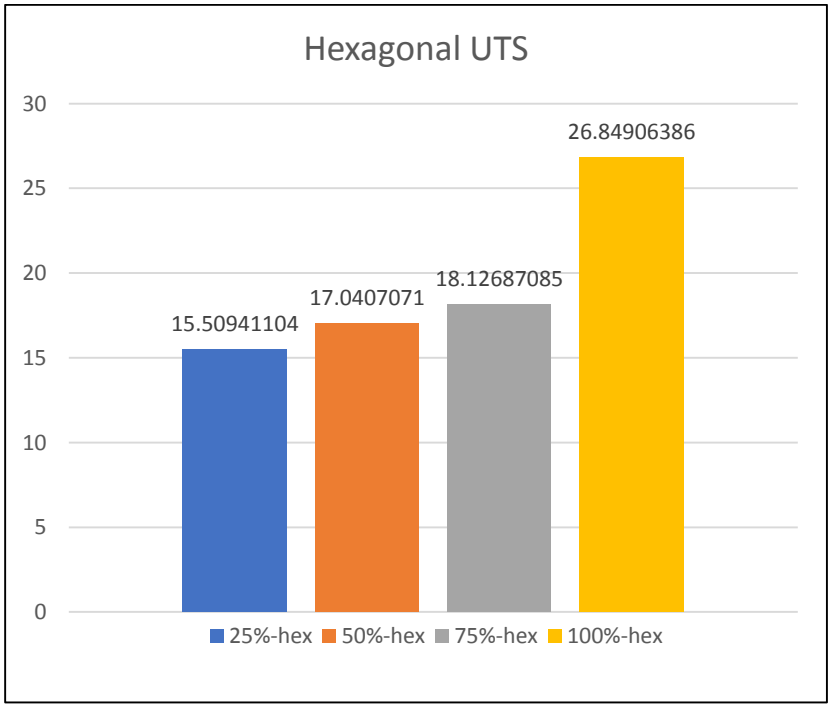

Figure 37: 2D histogram for UTS values of Hexagonal Shape Infill

The Permittivity vs. Frequency from the Di-electric test data for Linear shape infill with varying infill percentages is shown in figures [38-41]

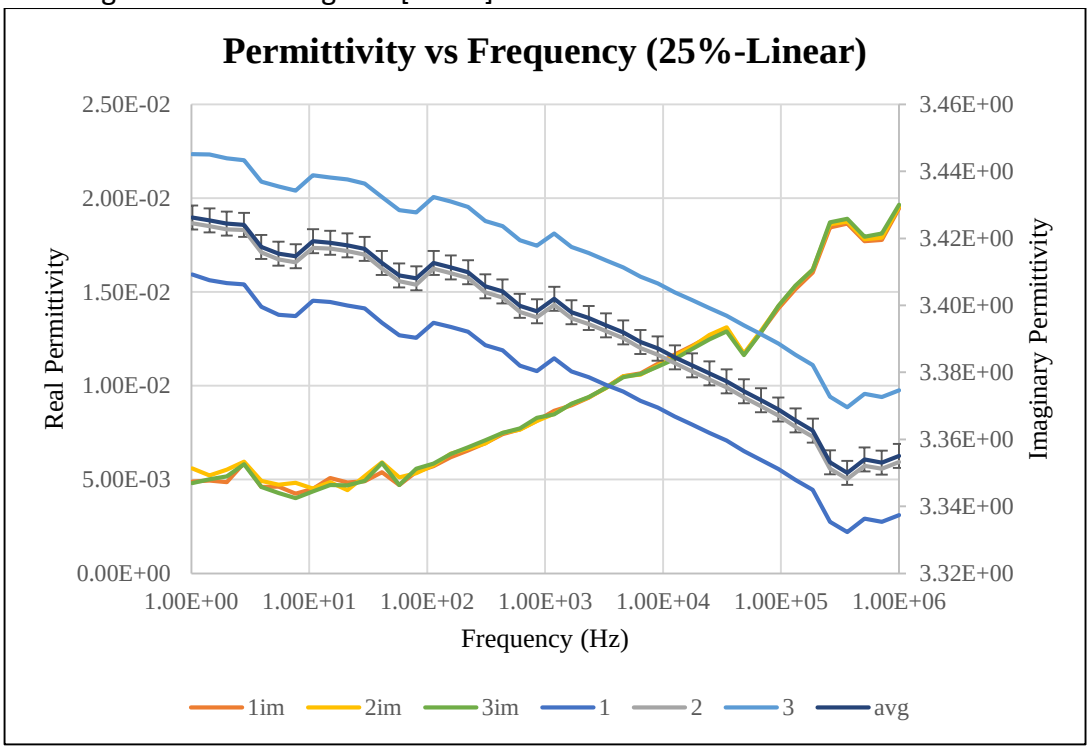

Figure 38: Permittivity vs. Frequency plots for 25% infill- Linear shape

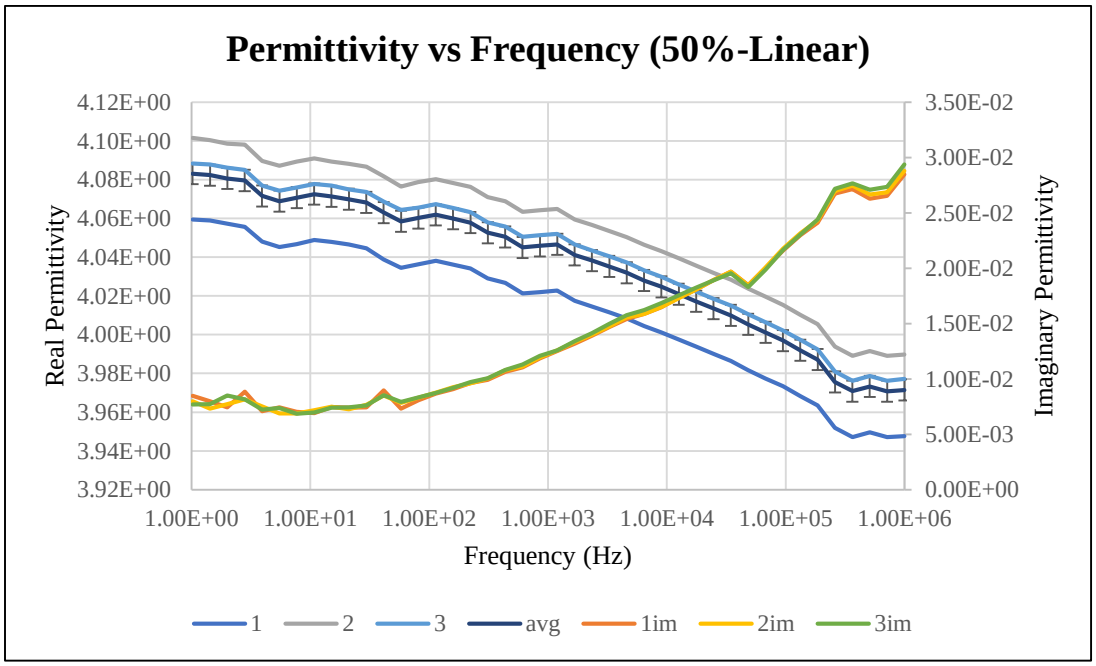

Figure 39: Permittivity vs. Frequency plots for 50% infill- Linear shape

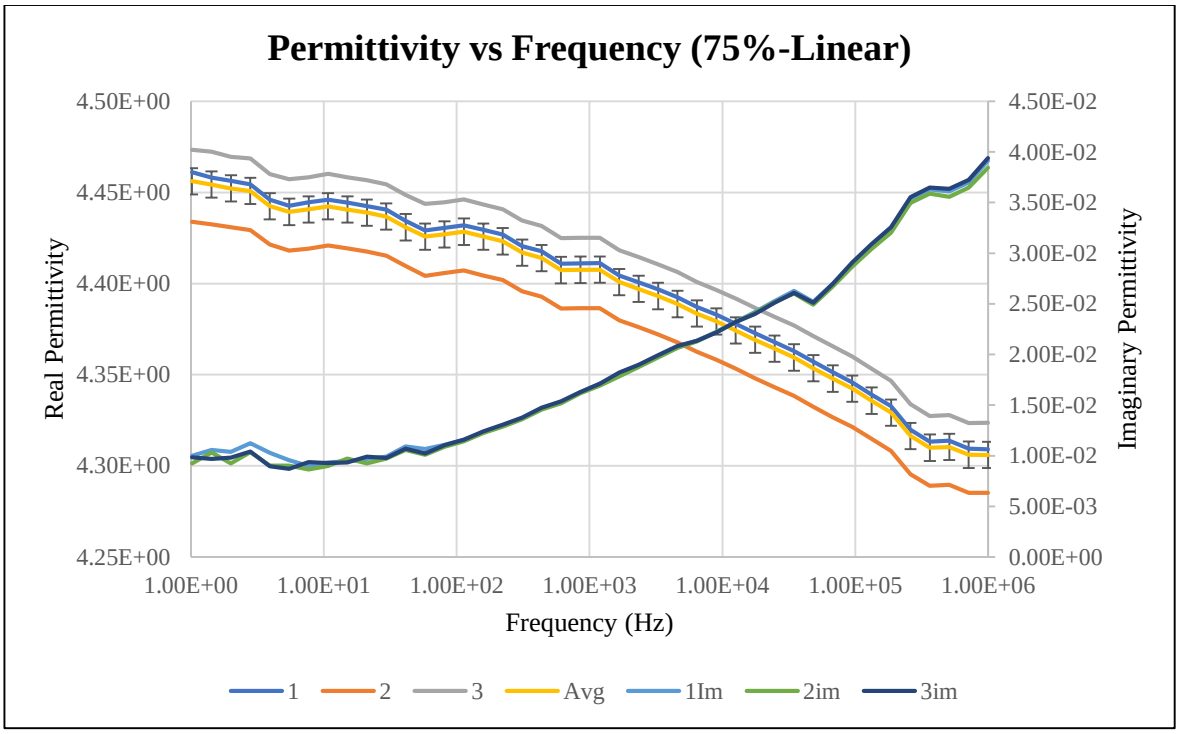

Figure 40: Permittivity vs. Frequency plots for 75% infill- Linear shape

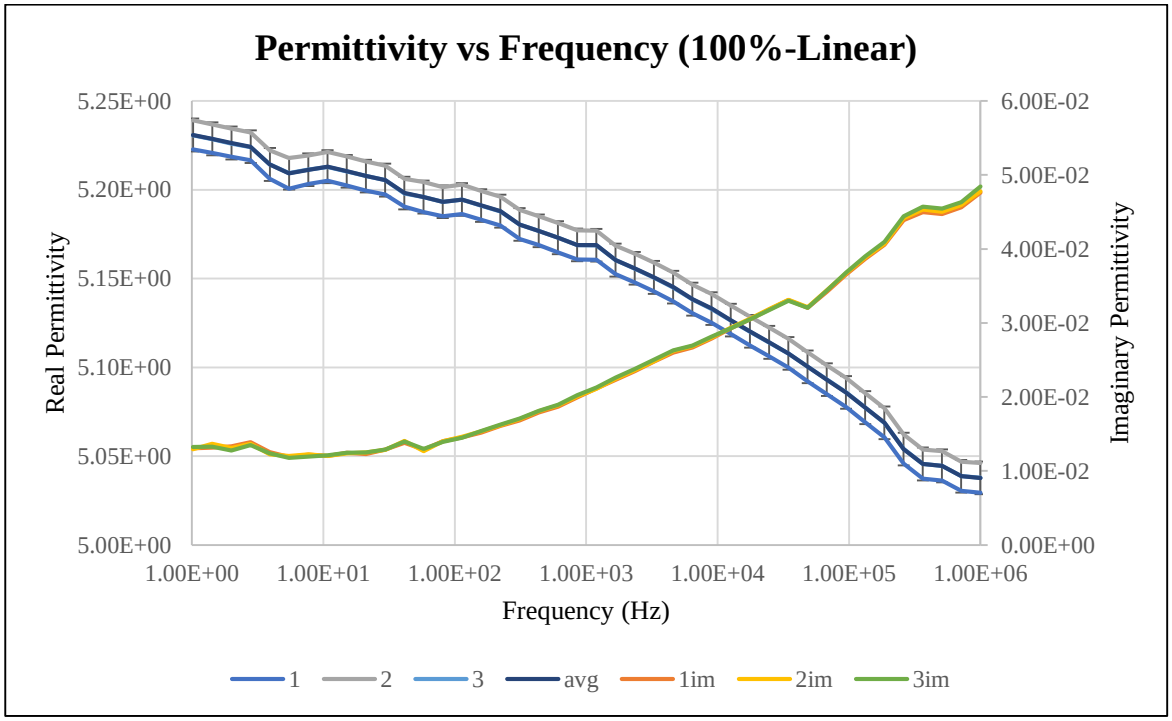

Figure 41: Permittivity vs. Frequency plots for 100% infill- Linear shape

The Permittivity vs. Frequency from the Di-electric test data for Diamond shape infill with varying infill percentages is shown in [42-45].

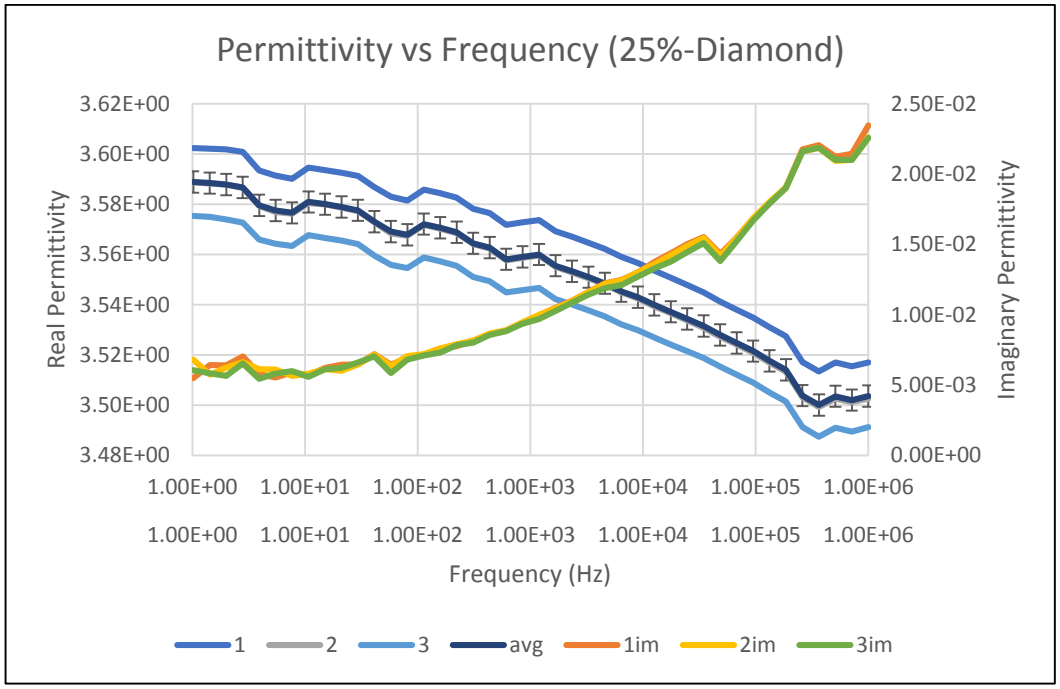

Figure 42: Permittivity vs. Frequency plots for 25% infill- Diamond shape

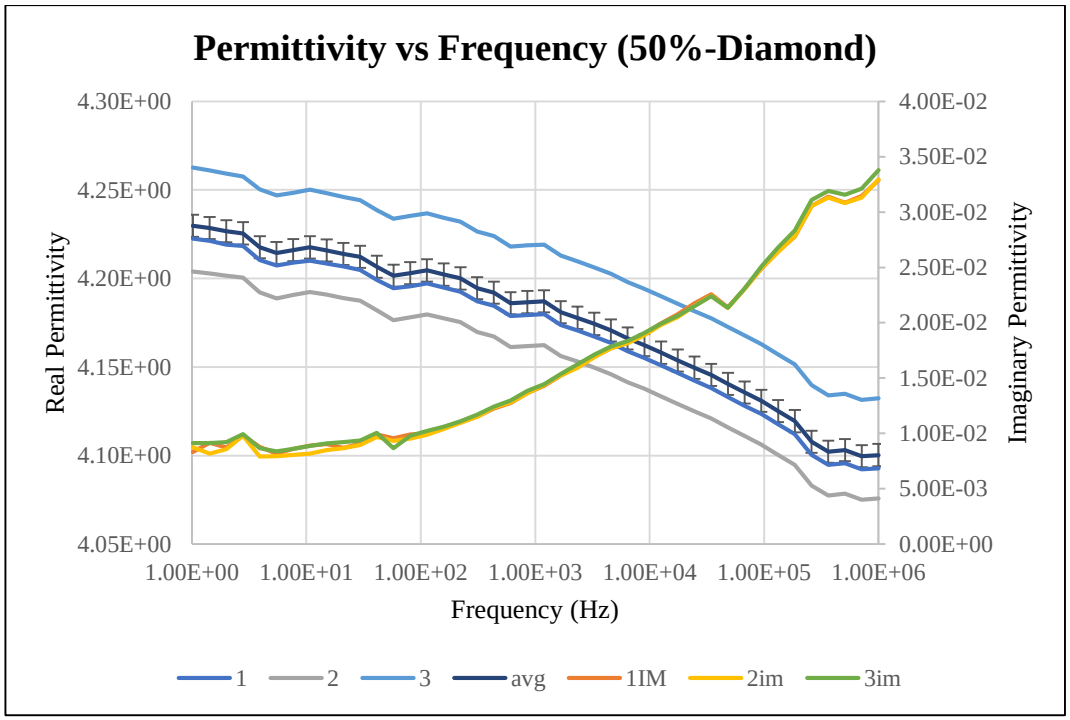

Figure 43: Permittivity vs. Frequency plots for 50% infill- Diamond shape

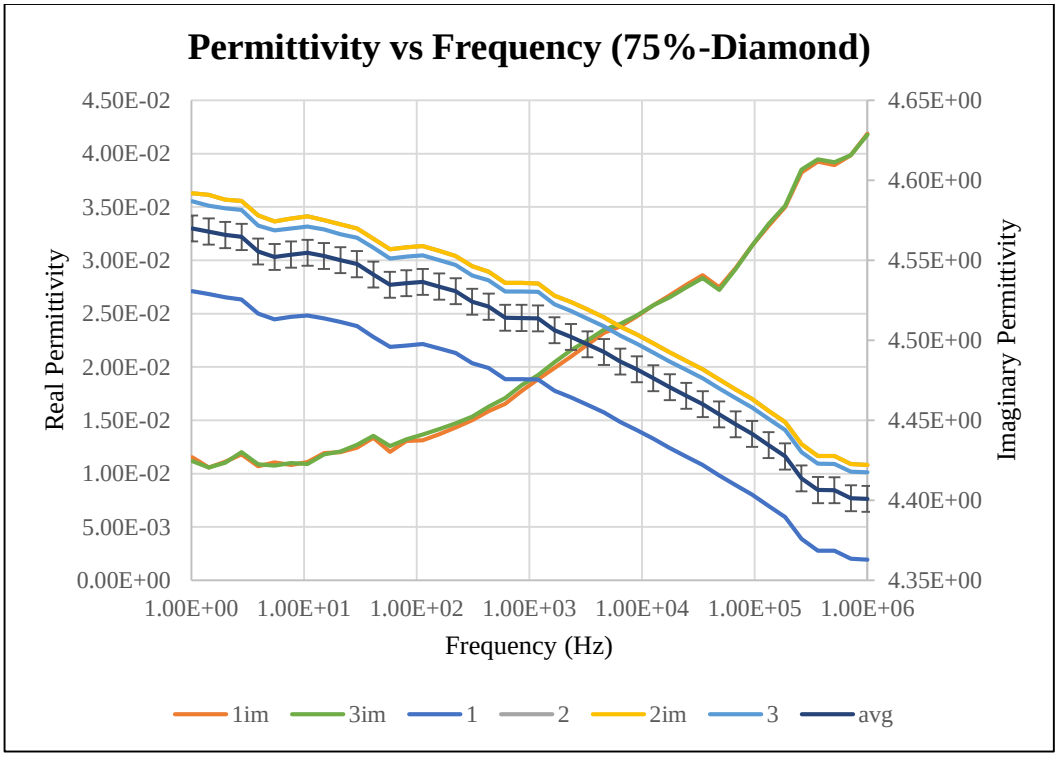

Figure 44: Permittivity vs. Frequency plots for 75% infill- Diamond shape

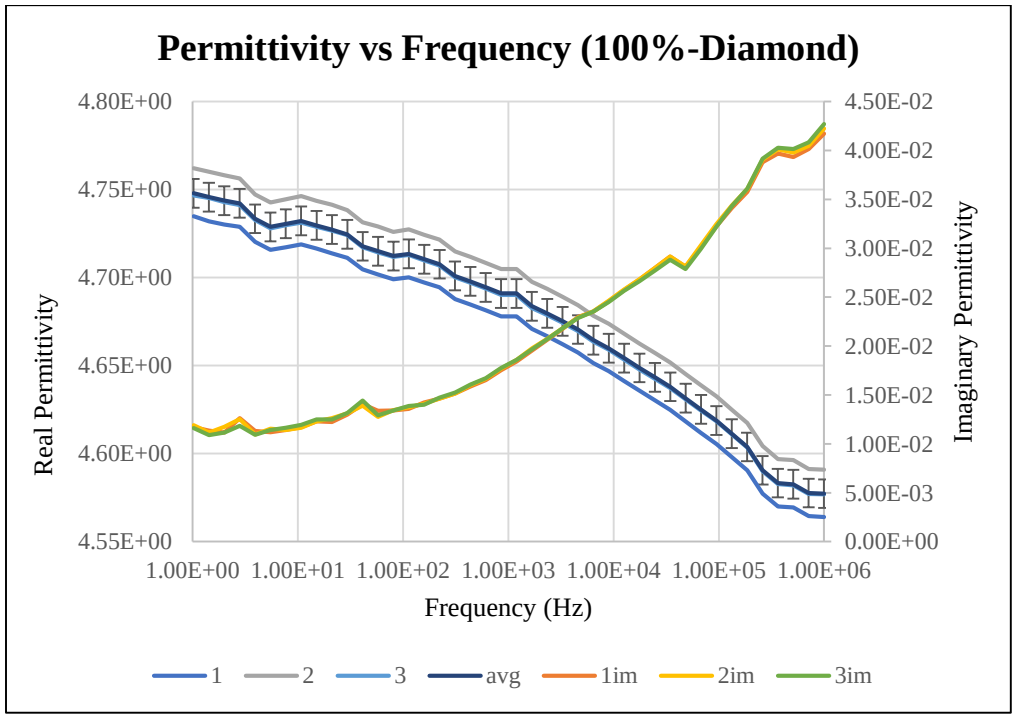

Figure 45: Permittivity vs. Frequency plots for 100% infill- Diamond shape

The Permittivity vs. Frequency from the Di-electric test data for Hexagonal shape infill with varying infill percentages is shown in [46-49].

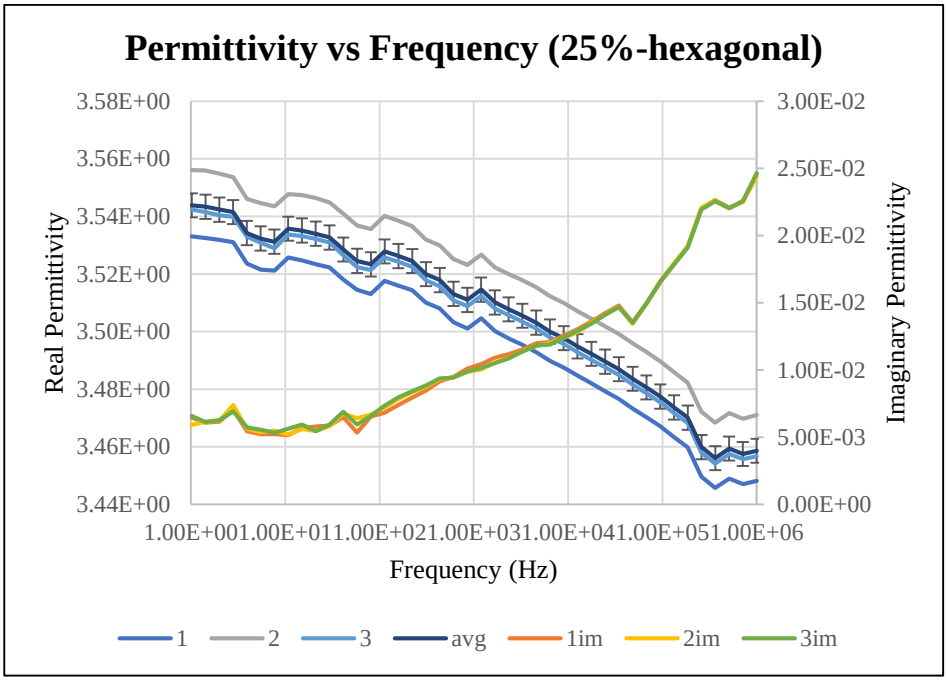

Figure 46: Permittivity vs. Frequency plots for 25% infill- Hexagonal shape

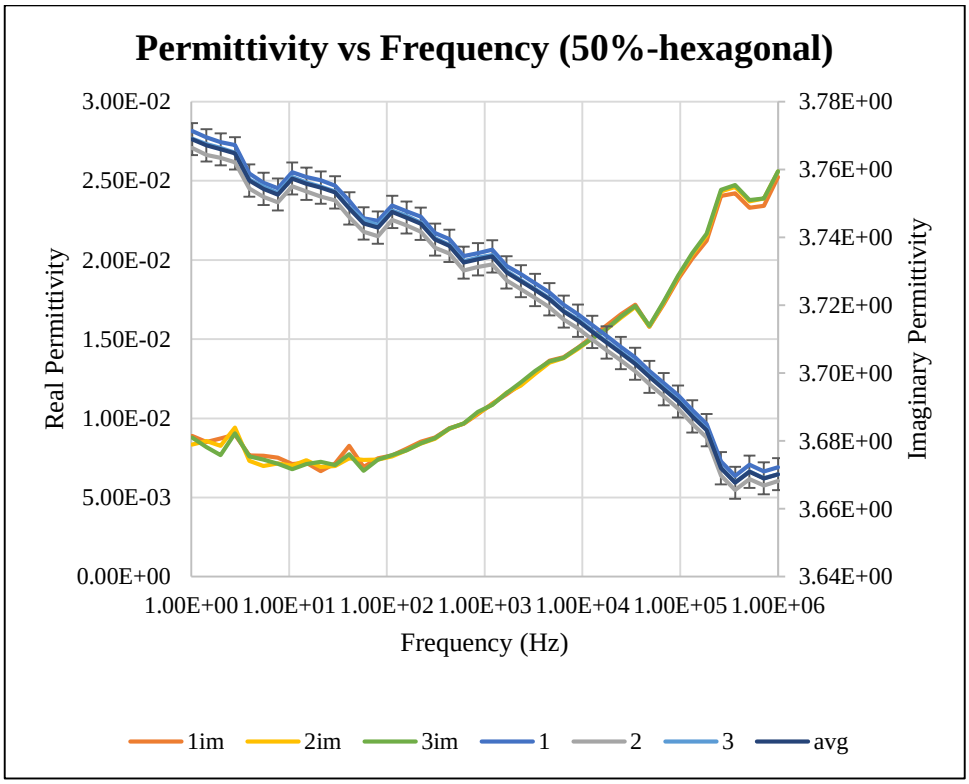

Figure 47: Permittivity vs. Frequency plots for 50% infill- Diamond shape

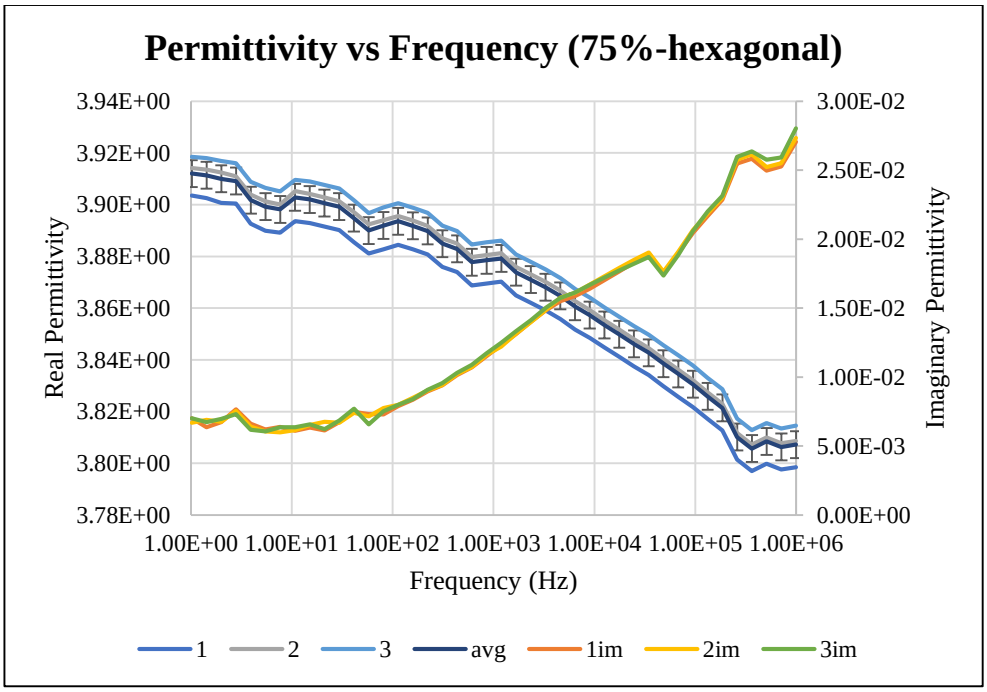

Figure 48: Permittivity vs. Frequency plots for 75% infill- Diamond shape

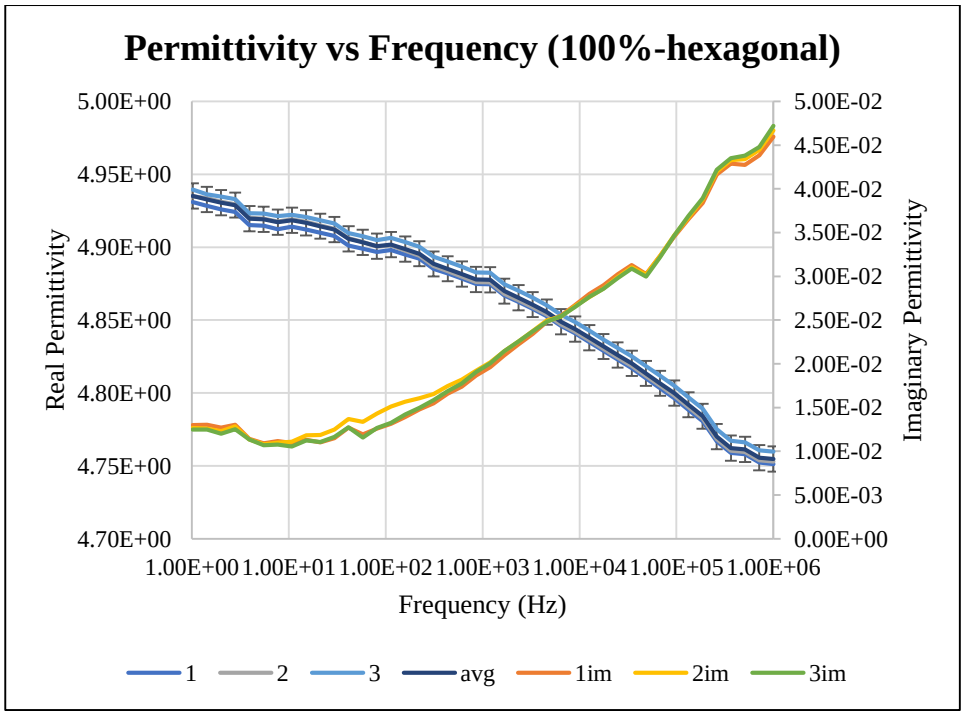

Figure 49: Permittivity vs. Frequency plots for 100% infill- Diamond shape

The average Di-electric Relaxation Strength (DRS) values for Linear, Diamond and Hexagonal shape infill with varying infill percentages is shown in figures [50-52].

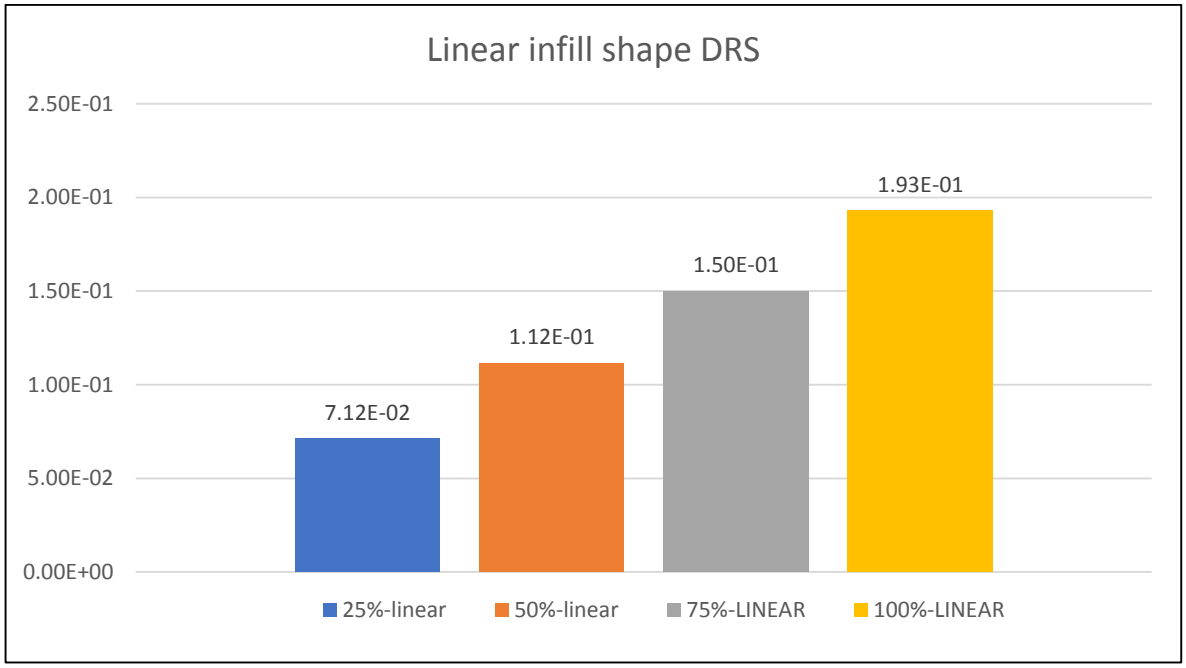

Figure 50: 2D Histogram for Average DRS values of linear shape infill with varying infill %

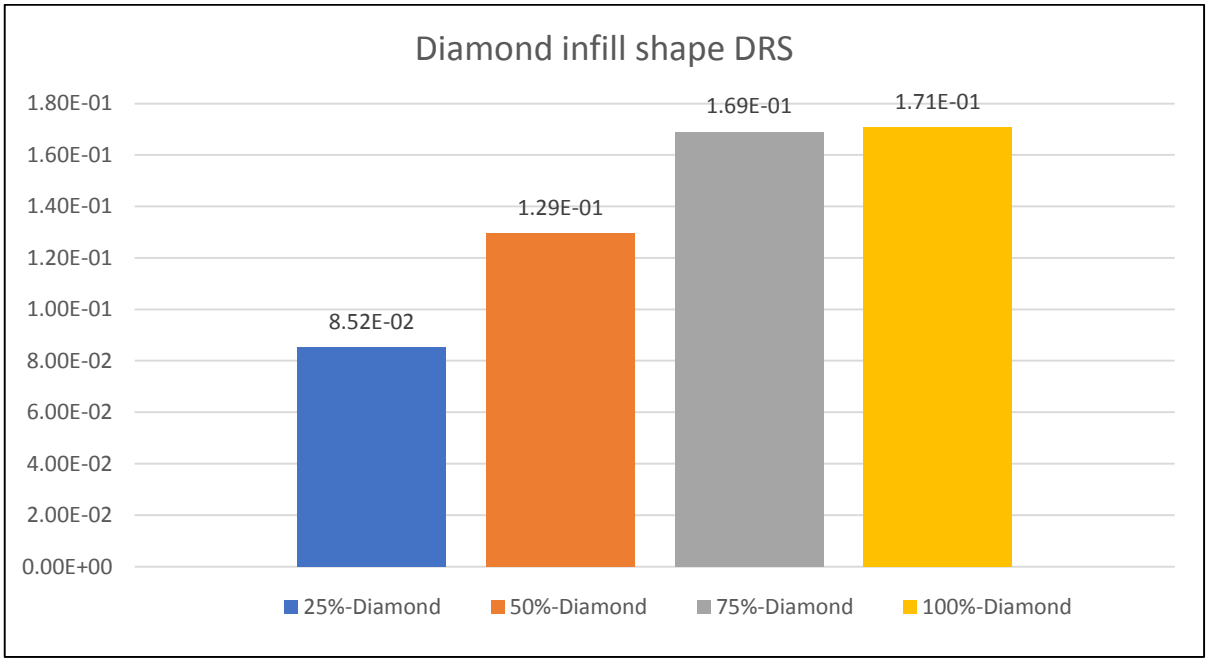

Figure 51: 2D Histogram for Average DRS values of Diamond shape infill with varying infill %

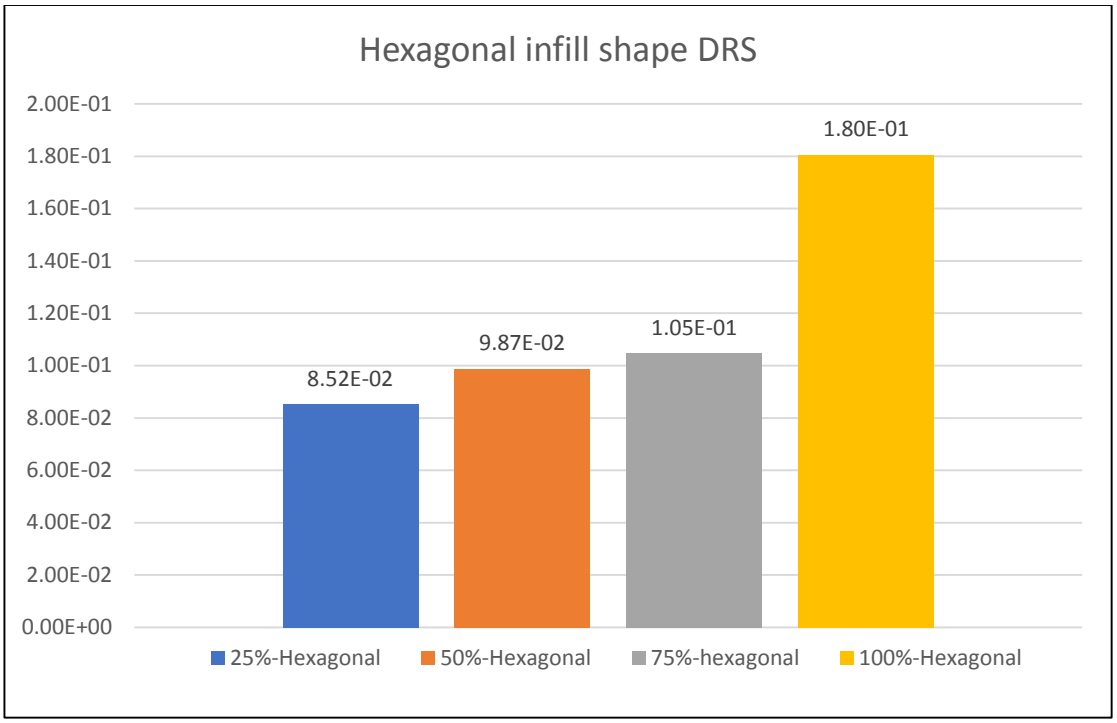

Figure 52: 2D Histogram for Average DRS values of Hexagonal shape infill with varying infill %

The crystallinity percentage was calculated for three different runs on the top and bottom sides of each sample from each set of the table 7 and average for these values was considered. The results are shown below in table 10.

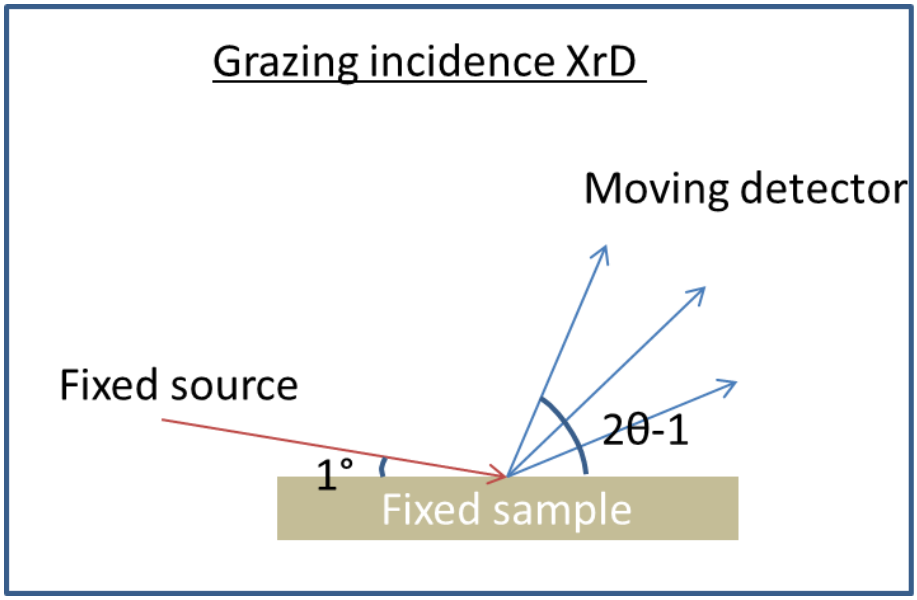

Figure 53: XRD Incidence on the sample

Table 10: Average Crystallinity percentage for each set in stage-2

Infill%	Pattern	Bottom	Top	Avg Crystallinity%
25	linear	19.031	18.5221	18.77653209
50	linear	16.5152	22.5942	19.55471903
75	linear	22.0667	18.3025	20.18461788
100	linear	17.0715	17.7821	17.42683101
25	diamond	17.0548	18.9117	17.9832488
50	diamond	20.5572	20.4749	20.51601297
75	diamond	20.5718	20.8347	20.70326567
100	diamond	21.882	22.9163	22.39913676
25	hex	17.7848	20.1761	18.98043407
50	hex	19.9948	20.9414	20.46809986
75	hex	22.013	22.2698	22.14137952
100	hex	24.234	22.4167	23.32538172

The Crystallinity % at the top and bottom surface of the sample was measured and the average was calculated as shown in figure 53 and Table 10. The **Average Crystallinity %** values of the bottom and top surface of each sample of each set is plotted as shown in figure 54.

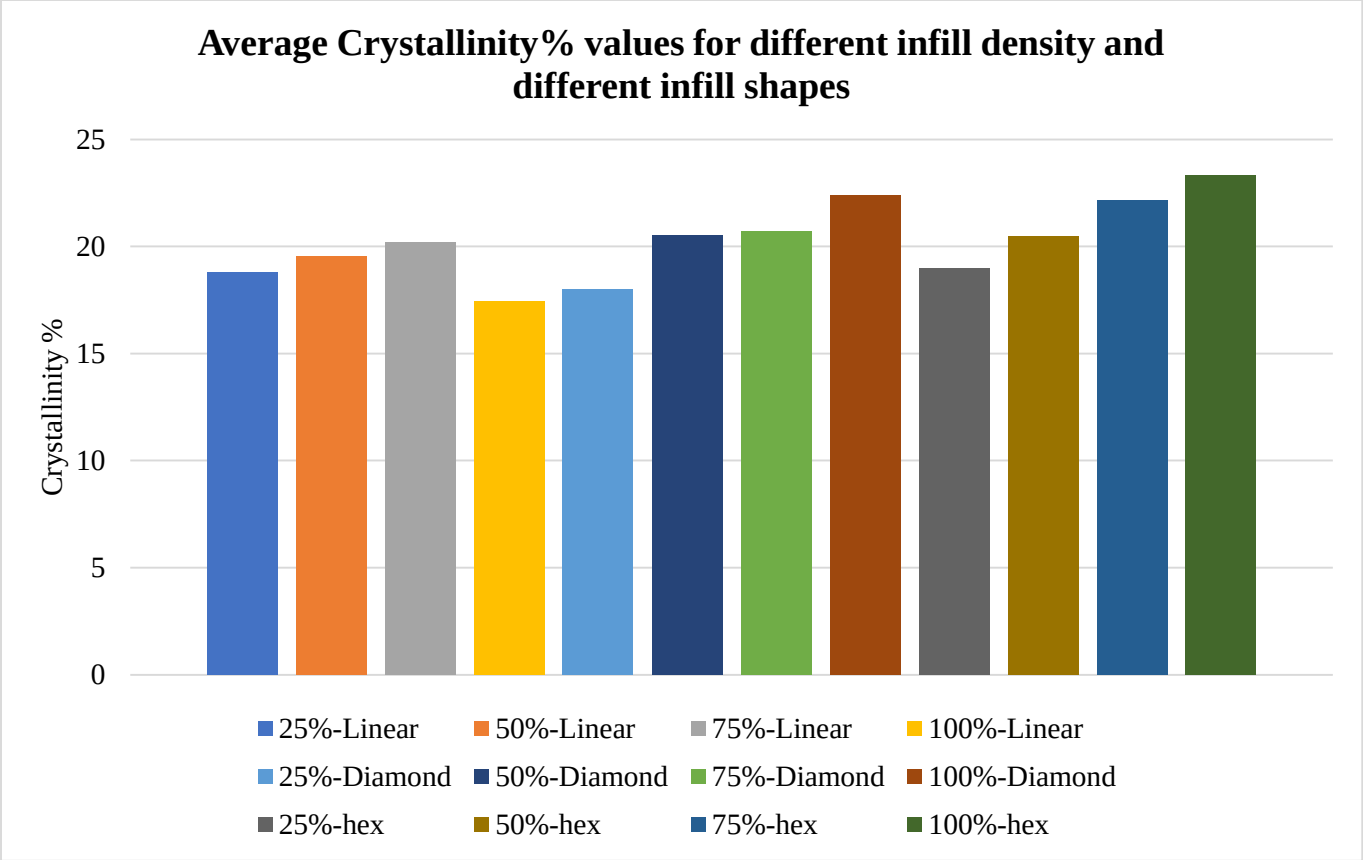

Figure 54: Average Crystallinity percentages for all the samples in Stage-2

Discussion:

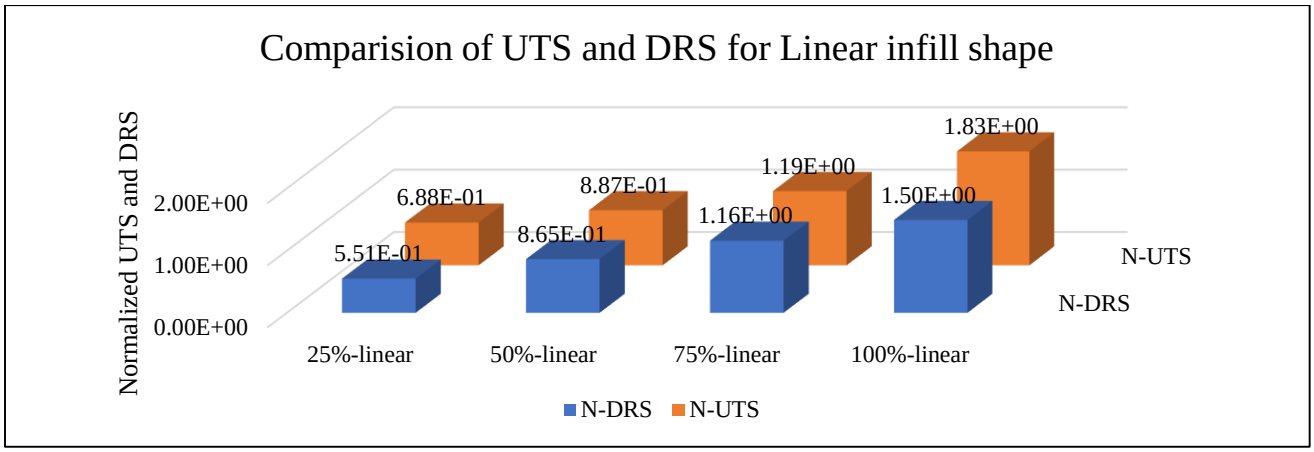

Figure 55: Comparison of UTS and DRS values for Linear Infill shape

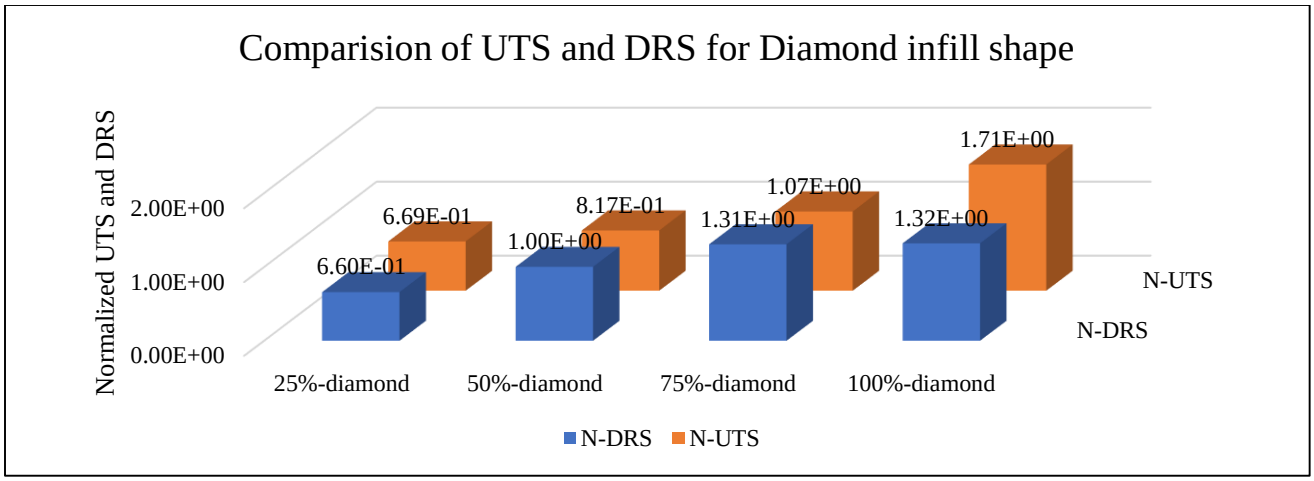

Figure 56: Comparison of UTS and DRS values for Diamond Infill shape

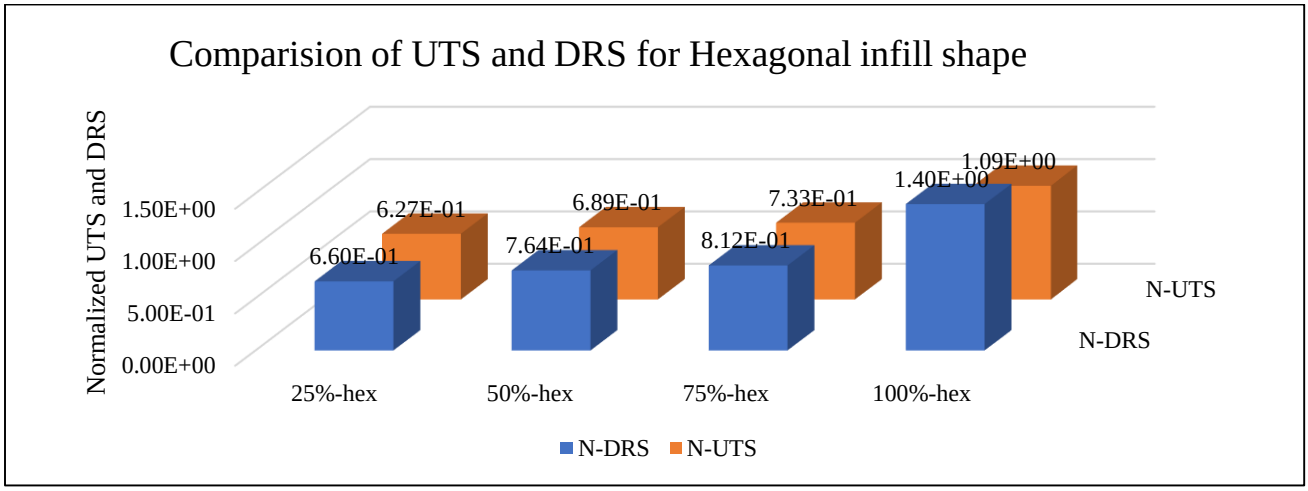

Figure 57: Comparison of UTS and DRS values for Hexagonal Infill shape

- From table 9 and figures [54-56] we observe that for Linear and Diamond Infill shape, the crystallinity % decreased at 100% infill. The hexagonal shape infill maintained higher crystallinity% even at 100% infill.
- From table 8 and figures [31, 33,35] the Ultimate Tensile Strength (UTS) and Di-electric Relaxation Strength (DRS) seem to maintain a trend even at different infill shapes and densities.
- From figures [58-60] we can see that there are reciprocative dips at identical frequencies in the Imaginary Permittivity vs. Frequency curves.

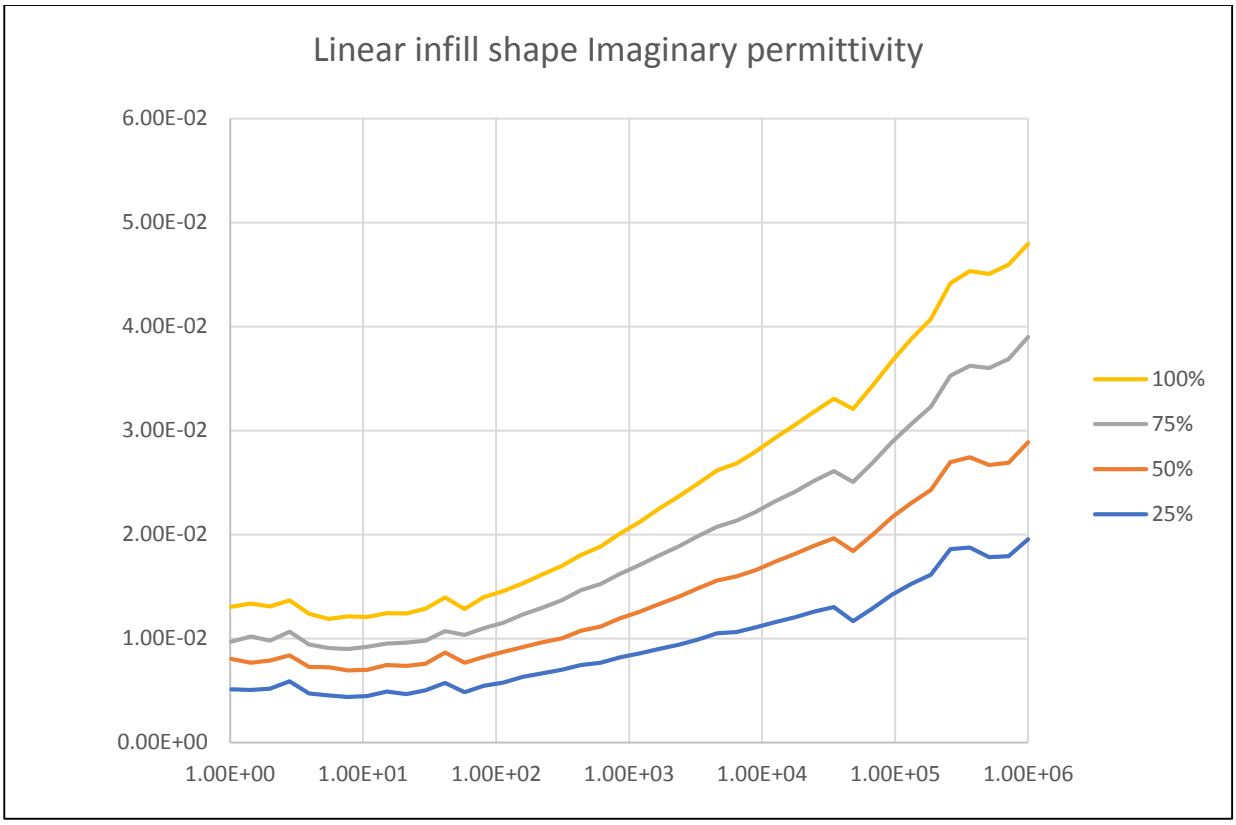

Figure 58: Imaginary Permittivity vs. frequency for Linear Infill Shape

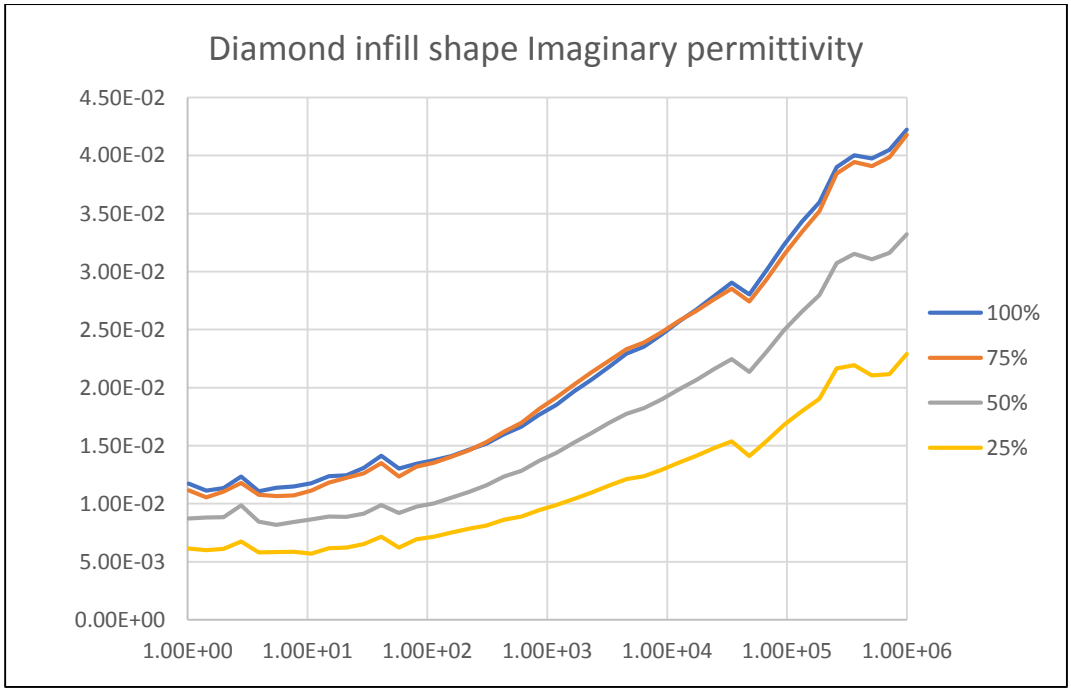

Figure 59: Imaginary Permittivity vs. Frequency for Diamond Infill shape

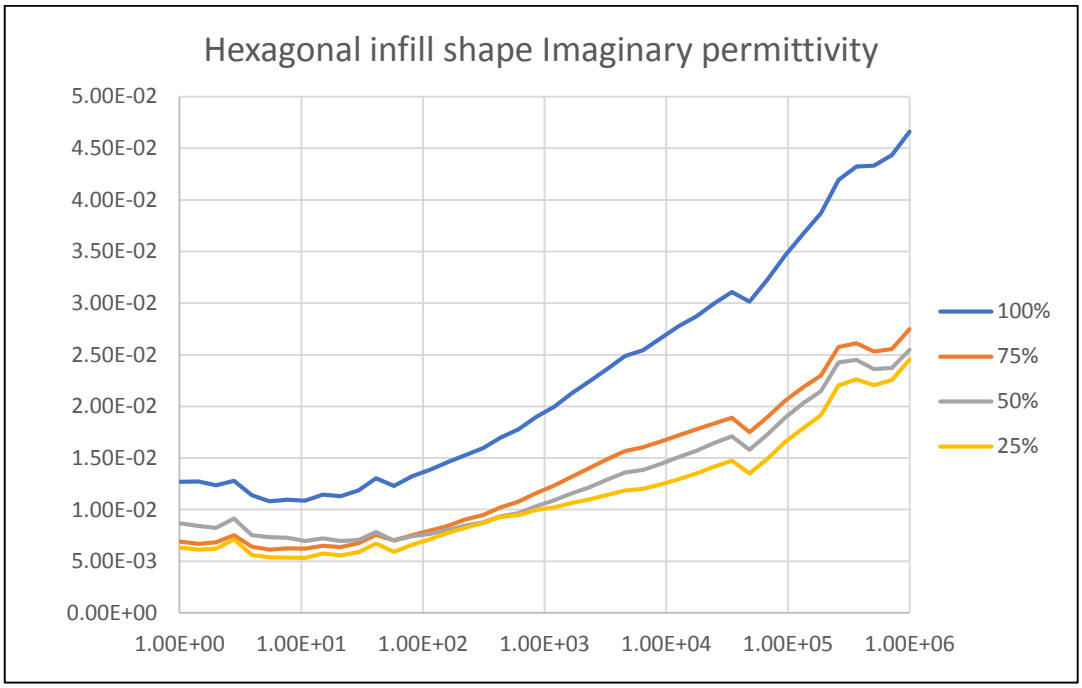

Figure 60: Imaginary permittivity vs Frequency for Hexagonal Infill shape

Conclusion

Before making any conclusions, let us take a final look at a summary of all the results obtained at Stage-1 and Stage-2.

Stage-1:

Table 11: Final results for Stage-1

Set	Infill %	Bed Temp (°C)	UTS (MPa)	DRS
1	12.5	50	20.62	0.04
2		75	20.63	0.102
3		80	20.034	0.038
4	33	50	23.627	0.05
5		75	23.136	0.02
6		80	22.8	0.03
7	50	50	26.203	0.05
8		75	26.02	0.03
9		80	24.78	0.033
10	100	50	49.833	0.16
11		75	48.62	0.03

To get a better understanding of these data, we can derive normalized plots for the above UTS and DRS values as shown below:

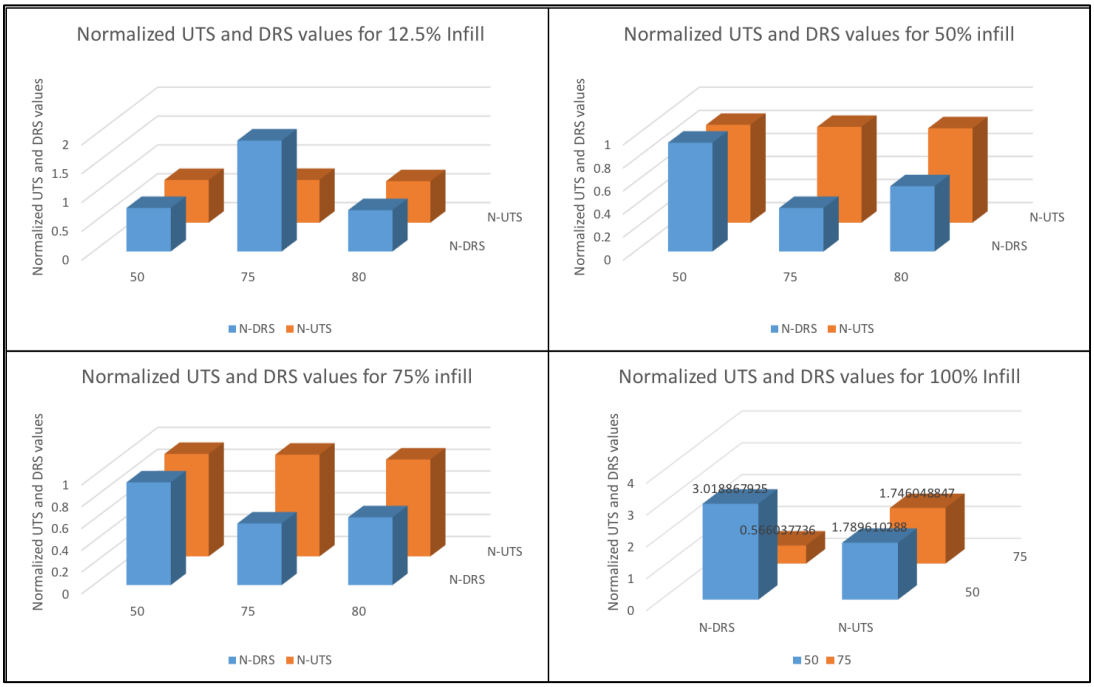

Figure 61: Normalized plots for average DRS and UTS values of different infill percentages at different bed temperatures

To attain normalized values of any data, we average all the data and divide each data value by the average. This will help us to plot Wide Ranged data in the same graph.

Looking at table 10 and figure 61 we may derive the following conclusions:

- At 80^0C Bed temperature, all the mechanical test samples seem to have reduced Ultimate Tensile Strength (UTS) values. This might have occurred due to the uncontrollable movement of the material while printing at high bed temperatures. We may assume that high temperatures cause **Warping,** a common term used for spiral material defects forming inside the printed structures.
- Another interesting observation would be the Ultimate Tensile Strength value of the 100% infill sample at 75^0C Bed Temperature. The value is lesser than that of the sample at 50^0C Bed Temperature. It can also be observed that 100% infill specimens have close to zero void spaces in their structure. This means that even at lower temperatures, an assumption can be made that the material would be restricted to move in a 100% infill specimen due to lack of gaps. This may lead to internal stresses that in turn effect the Ultimate Tensile Strength of the specimen.
- To confirm these assumptions, further research was required, which led to Stage-2 part of the thesis.

Stage-2:

Table 12:Table of all final results from Stage-2

Set	Avg UTS	Avg DRS	Avg Crystallinity %
25%-linear	17.02552	7.12E-02	18.77653209
50%-linear	21.93299	1.12E-01	19.55471903
75%-linear	29.52417	1.50E-01	20.18461788
100%-linear	45.24648	1.93E-01	17.42683101
25%-diamond	16.54561	8.52E-02	17.9832488
50%-diamond	20.20971	1.29E-01	20.51601297
75%-diamond	26.54912	1.69E-01	20.70326567
100%-diamond	42.21658	1.71E-01	22.39913676
25%-hex	15.50941	8.52E-02	18.98043407
50%-hex	17.04071	9.87E-02	20.46809986
75%-hex	18.12687	1.05E-01	22.14137952
100%-hex	26.84906	0.180473333	23.32538172

For better understanding, we normalize the average of the DRS and UTS and crystallinity % values of each set and plot as shown in Figures [58-60]. Looking at the table and figure we may derive the following conclusions:

- The first thing we notice after looking at the normalized plots is that the Di-electric Relaxation Strength (DRS) and Ultimate Tensile Strength (UTS) seem to be following a trend. This can be derived into a relation where they are directly proportional to each other.

$$DRS \; \alpha \; UTS \tag{15}$$

- Referring to Table 11, there is mostly a constant trend in the average crystallinity % for the specimens. It can also be observed that the average crystallinity percentage for 100% infill specimens with Linear and Diamond infill shape deviated from the trend (the values were less than that of 75% infill for their respective morphologies). Before coming to a conclusion let us also look at the length of elongation break for all the samples from figures [31,33,35].

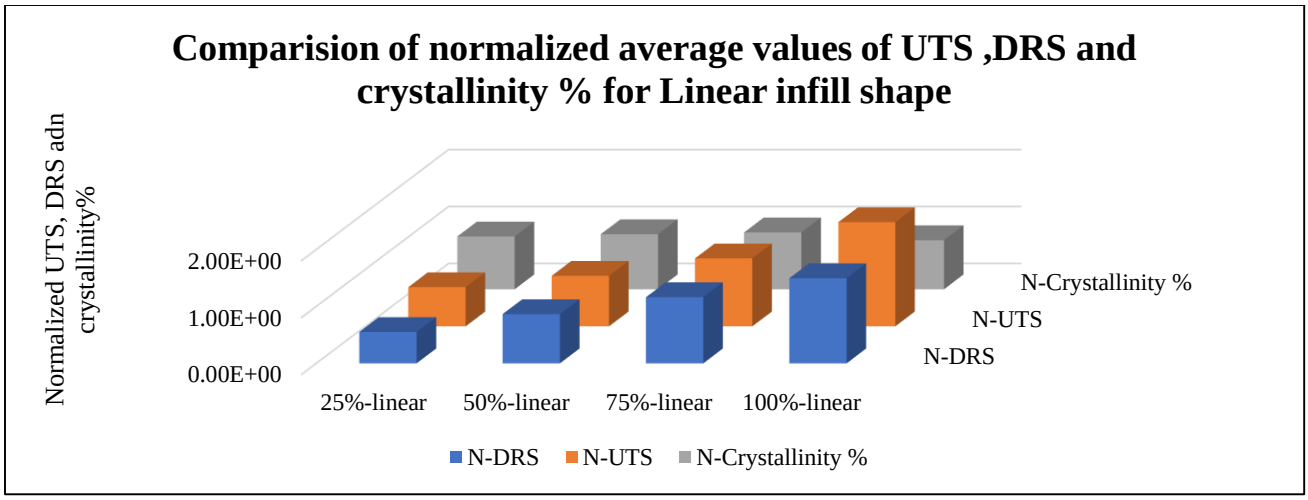

Figure 62: Normalized plots for Linear infill shape at varying infill %

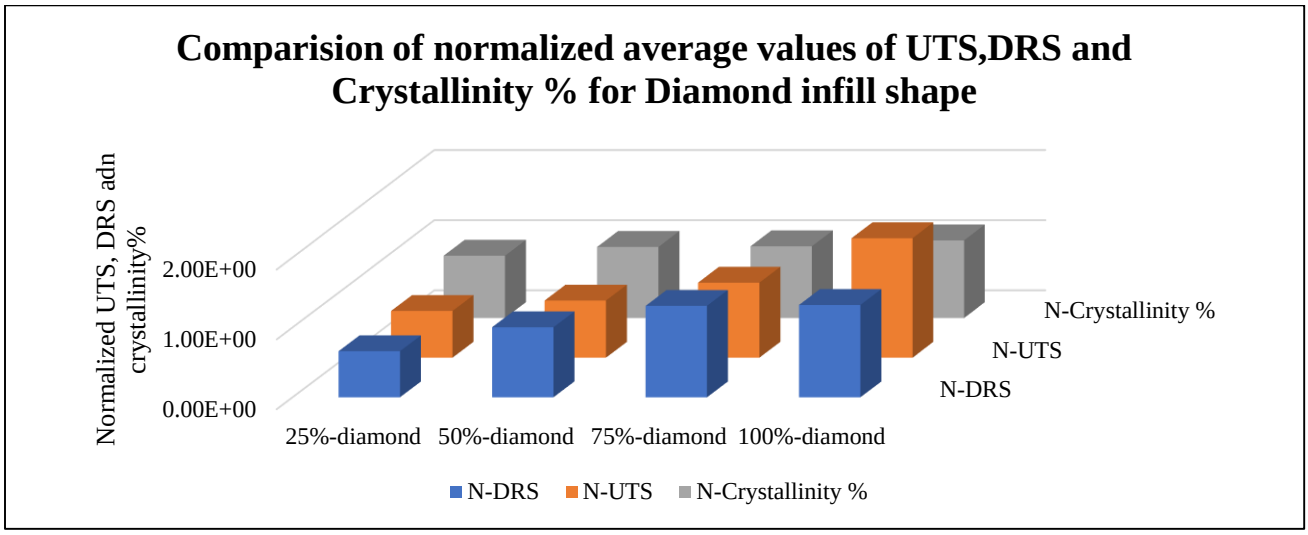

Figure 63: Normalized plots for diamond Infill shape at varying infill %

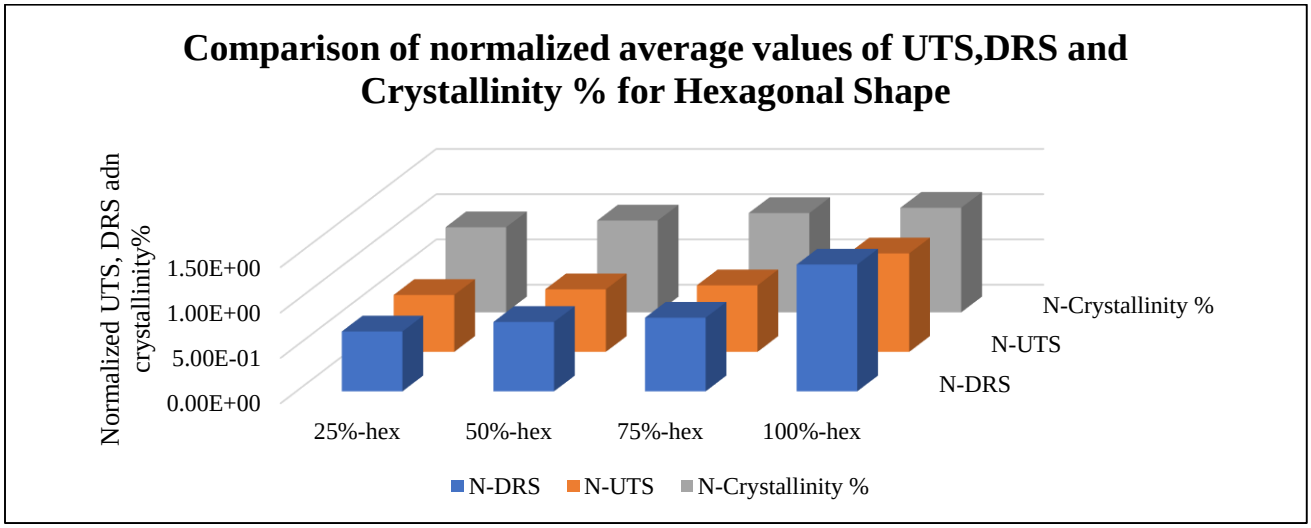

Figure 64: Normalized plots for Hexagonal Infill shape at varying infill %

It can be observed from the figures [31,33,35] that the length of elongation break is also less for 100% infill- Linear and diamond shape specimens compared to the hexagonal 100% infill specimen, that maintained its high elongation length.

Going back to the assumptions we made in stage-1:

(1) At high temperatures cause warping due to uncontrollable movement of the material inside the structure.

(2) Even at lower temperatures with high infill percentage, the material would be restricted to move in a 100% infill specimen due to lack of gaps. This may lead to internal stresses that in turn effect the Ultimate Tensile Strength of the specimen.

Going back to [16] to derive our final conclusions:

- Higher infill percentage leads to development of internal stresses which make it weaker.
- The lower crystallinity percentage for 100 % infill samples is due to the lack of gaps, thereby preventing the growth of crystals.
- The Di-electric Relaxation Strength is directly proportional to the Ultimate Tensile Strength.

Future Work

The future work for this thesis can be given the following directions:

- Multi-physics analysis of 3D Printed PLA by using its Mechanical and Di-electric data.
- Research on other Di-electric data and their relationship with manufacturing parameters.
- Exploring crystallinity of other 3D printable materials such as Carbon fiber reinforced thermoplastics.
- SEM study on the fracture surfaces of the Mechanical test specimens, to further understand the stacking structural properties of 3D printed materials.

References

1) AM Basics. (2018). Additive Manufacturing Amazing.
2) Gibson, I., Rosen, D., & Stucker, B. (2010). *Additive Manufacturing Technologies,3D Printing, Rapid Prototyping and Direct Digital Manufacturing.*
3) Benwood, C., Anstey, A., Andrzejewski, J., & K.Mohanty, M. M. (n.d.). *Improving the Impat strength and heat resistance of 3D printed Models: Structure,Property,and processing Correlationships during FDM of Poly(Lactic Acid).*
4) Pearce, J., Morris Blair, C., Laciak, K., Andrews, R., Nosrat, A., & Zelenika-Zovko, I. (2010). *3D printing of Open Source Appropriate Technologies for Self Directed Sustainable Development. In J.Sustainable Dev (pp. 17-29).*
5) Huang, S., Liu, P., Mokasdar, A., & Hou, L. (2013). *Additive Manufacturing and its Societal Impact: A Litearture Review. Int.J.Adv.MAnuf.Technol, 1191-1203.*
6) Bates-Green, K., & Howie, T. (n.d.). *Materials for 3D printing by Fused Deposition.*
7) Lopes, M., Jardini, A., & Filho.R. (2014). *Synthesis and characterizations of poly(lactic acid) by ring-opening polymerization for biomedical applications. Chemical Engineering Transactions, 331-336.*
8) Wittbrodt, B., & Pearce, J. M. (n.d.). *The effects of PLA color on material properties of 3D printed components.*
9) Williams, C. (2018). *Are 3D Printed Buildings a Cost-Saving Solution for developers.* Retrieved from BISNOW: https://www.bisnow.com/national/news/construction-development/3d- printed-buildings-a-fad-or-a-viable-cost-saving-solution-for-developers-87022?utm_source=CopyShare&utm_medium=Browser
10) ROBSON, J. (2018, AUGUST). *Crystallinity and Filaments. Retrieved from Filaments.*Directory:https://www.filaments.directory/en/blog/2018/08/01/crystallinity-and-filaments
11) H.Tsuji, & Y.Ikada. (1995). *Polymer.*
12) A., S., & F., K. (2003). *Broadband Dielectric Spectroscopy. Berlin,Heidelberg: Springer.*
13) Banerjee, P., Elenchezian, M., Vadlamudi, V., Raihan, R., & and Reifsnider, K. (2017). *Predicting Adhesive Bond Performance Based on Initial Dielectric Properties. American society for composites.*

14) Raihan, R., Adkins, J., Baker, J., Rabbi, F., & and Reifsnider, K. (2015). *Relationship of Di-electric property change to composite material state degradation. Composite Sciences and Technology, 160-165.*

15) Reifsnider, K., Raihan, M., & and Vadlamudi, V. (n.d.). *Heterogeneous fracture mechanics for multi-defect analysis. Composite Structures, 20-28.*

16) Claudius Dichtl, P. S. (n.d.). Di-electric Properties of 3D printed Polylactic Acid.

17) Als-Nielsen, J., & McMorrow, D. (2011). *Elements of modern X-ray physics*. John Wiley & Sons.

18) O'Neal, B. (2015). *3DMatter Researches Effects of Infill Percentages, Patterns, and Layer Height on 3D Printed Structures*. Retrieved from 3DPRINT.COM: https://3dprint.com/51065/infill-percentages-3d-printing/

19) ASTM D638-14 *Standard test Method for Tensile Properties of Plastics. (n.d.). ASTM International.*

20) Munaganuru, S. S. N., Elenchezhian, M. R. P., Vadlamudi, V., Shaik, R. A., Adluru, H. K., Raihan, R., & Reifsnider, K. (2018). Effects of Build Parameters on the Mechanical and Di-Electrical Properties of AM parts. *Solid Freeform Fabrication 2018: Proceedings of the 29th Annual International Solid Freeform Fabrication Symposium–An Additive Manufacturing Conference.*

21) Retrieved from MOST, *XRD(X-ray Diffraction Protocol): http:// www.appropedia.org/XRD (X-ray Diffraction) protocol: MOST(2014).*

22) Dizon, J., Espera, A., Chen, Q., & and Advincula, R. (2017). *Mechanical characterization of 3D Printed PLA. Additive Manufacturing.*